INVESTIGATING QUANTUM DATA ENCRYPTED MODULATION STATES

NOVEMBER 2014

INTERIM TECHNICAL REPORT

APPROVED FOR PUBLIC RELEASE; DISTRIBUTION UNLIMITED

STINFO COPY

AIR FORCE RESEARCH LABORATORY
INFORMATION DIRECTORATE

■ **AIR FORCE MATERIEL COMMAND**   ■   **UNITED STATES AIR FORCE**   ■   **ROME, NY 13441**

NOTICE AND SIGNATURE PAGE

AFRL-RI-RS-TR-2014-280   HAS BEEN REVIEWED AND IS APPROVED FOR PUBLICATION IN ACCORDANCE WITH ASSIGNED DISTRIBUTION STATEMENT.

FOR THE DIRECTOR:

/ S /   **/ S /**

RICHARD MICHALAK   MARK H. LINDERMAN
Chief, Information Transmission Branch   Technical Advisor
                                                                  Computing & Communications Division
                                                                  Information Directorate

REPORT DOCUMENTATION PAGE

Form Approved
OMB No. 0704-0188

1. REPORT DATE *(DD-MM-YYYY)* NOVEMBER 2014	2. REPORT TYPE INTERIM TECHNICAL REPORT	3. DATES COVERED *(From - To)* OCT 2013 – OCT 2014

4. TITLE AND SUBTITLE INVESTIGATING QUANTUM DATA ENCRYPTED MODULATION STATES	5a. CONTRACT NUMBER IN-HOUSE / R148
	5b. GRANT NUMBER N/A
	5c. PROGRAM ELEMENT NUMBER 61102F
6. AUTHOR(S) Paul Cook, David Legare, David Hummel, John Malowicki, David H. Hughes, Reinhard Erdmann	5d. PROJECT NUMBER TIQD
	5e. TASK NUMBER IN
	5f. WORK UNIT NUMBER H0

7. PERFORMING ORGANIZATION NAME(S) AND ADDRESS(ES) Air Force Research Laboratory/Information Directorate Rome Research Site/RITE 525 Brooks Road Rome NY 13441-4505	8. PERFORMING ORGANIZATION REPORT NUMBER N/A

9. SPONSORING/MONITORING AGENCY NAME(S) AND ADDRESS(ES) Air Force Research Laboratory/Information Directorate Rome Research Site/RITE 525 Brooks Road Rome NY 13441-4505	10. SPONSOR/MONITOR'S ACRONYM(S) AFRL/RI
	11. SPONSORING/MONITORING AGENCY REPORT NUMBER AFRL-RI-RS-TR-2014-280

12. DISTRIBUTION AVAILABILITY STATEMENT
Approved for Public Release; Distribution Unlimited. PA# 88ABW-2014-5150
Date Cleared: 6 Nov 2014

13. SUPPLEMENTARY NOTES

14. ABSTRACT
AFOSR LRIR13RI08COR supports four related efforts, all primarily concerned with aspects of optical communications. However, some of our efforts also include the RF spectrum in that we are working toward a combined optical/RF link operating between our site in Rome NY and Stockbridge NY. We leverage AFRL 6.2 funds as well. AFOSR FY 2014 funds were largely devoted to salary for government and onsite contractors. Some funds have been used for equipment purchases. Section 2 reports on basic research into noise corrupting phase estimation in coherent states of light in the 1.5 micron band. Section 3 reports on a comparative study between long wavelength infrared (LWIR) versus short wavelength infrared (SWIR) propagation in fair and inclement weather. Section 4 reports on the combined optical/RF link work under way between Stockbridge and Rome. Section 5 characterizes the propagation of entangled photon pairs through a hyper spectral filter device originally designed for multi-access laser communications between a hub and multiple spokes.

15. SUBJECT TERMS

Coherent optical detection, Long wavelength infrared, combined optical/RF link, entangled photon pairs, Lyot filter

16. SECURITY CLASSIFICATION OF:			17. LIMITATION OF ABSTRACT	18. NUMBER OF PAGES	19a. NAME OF RESPONSIBLE PERSON **DAVID H. HUGHES**
a. REPORT U	b. ABSTRACT U	c. THIS PAGE U	SAR	67	19b. TELEPHONE NUMBER *(Include area code)* **N/A**

Standard Form 298 (Rev. 8-98)
Prescribed by ANSI Std. Z39.18

Table of Contents

List of Figures

List of Tables

1 Program Overview

LRIR13RI08COR

Title: Investigating Quantum Data Encrypted Modulation States

Reporting Period: FY14

Laboratory Task Manager: Dr. David H. Hughes

Commercial Phone:315-330-4122   DSN:587-4122

E-Mail Address: david.hughes.16@us.af.mil

AFOSR Program Manager: Dr. Arje Nachman

Research Objectives: Investigate and measure modulated optical signals, both quantum and classical, for Information confidentiality, integrity, and availability

1.1 Introduction

AFOSR LRIR13RI08COR supports four related efforts, all primarily concerned with aspects of optical communications. However, some of our efforts also include the RF spectrum in that we are working toward a combined optical/RF link operating between our site in Rome NY and Stockbridge NY. We leverage AFRL 6.2 funds as well. AFOSR FY 2014 funds were largely devoted to salary for government and onsight contractors. Some funds have been used for equipment purchases. A breakdown of the spending is given in Table 1 below.

1.2 Technical Work

Section 2 reports on basic research into noise corrupting phase estimation in coherent states of light in the 1.5 micron band. Over and above the quantum noise of light, with which recent physical cryptographic systems utilize to impart randomness to a ciphertext, additional noise sources can have an even more debilitating effect on attempts to decrypt ciphertext. These latter sources of noise include detection system thermal noise as well as source laser phase drift noise.

Section 3 reports on a basic comparative study between long wavelength infrared (LWIR) versus short wavelength infrared (SWIR) propagation in fair and inclement weather. Currently the communication bands under study are 1.5 and 10 micron bands. Despite the huge infrastructure devoted to the 1.5 micron band, work in the 10 micron band by several workers, including AFRL/RITE engineers, indicates that propagation in the 10 micron band is more robust in free space optics. That translates to greater information availability.

Section 4 reports on the combined optical/RF link work under way between Stockbridge and Rome. Currently, the optical band is primarily 1.5 micron band carrier frequencies; turbulence mitigation is accomplished by curvature adaptive optics. Planned is deployment of the LWIR/SWIR comparison experiment system over the longer range provided by the Rome/Stockbridge link as well as a coherent state quantum data encryption system.

Section 5 characterizes the propagation of entangled photon pairs through a hyperspectral filter device originally designed for multi-access laser communications between a hub and multiple spokes. We asked the question: Is polarization entanglement preserved in transit through the device? If not, can the device be modified to preserve the entanglement?

Table 1. Resource Dispersal FY14

Government Salaries	$107,000
Onsite Contractor Support	$99,640
Equipment	$73,360
Total	$280,000

2 Coherent State Phase Estimation

(Mr. Paul Cook)

2.1 Introduction and Background: Expected Results via Theory and Simulation

The estimation of phase will be carried out by heterodyne and homodyne methods. The signal will be
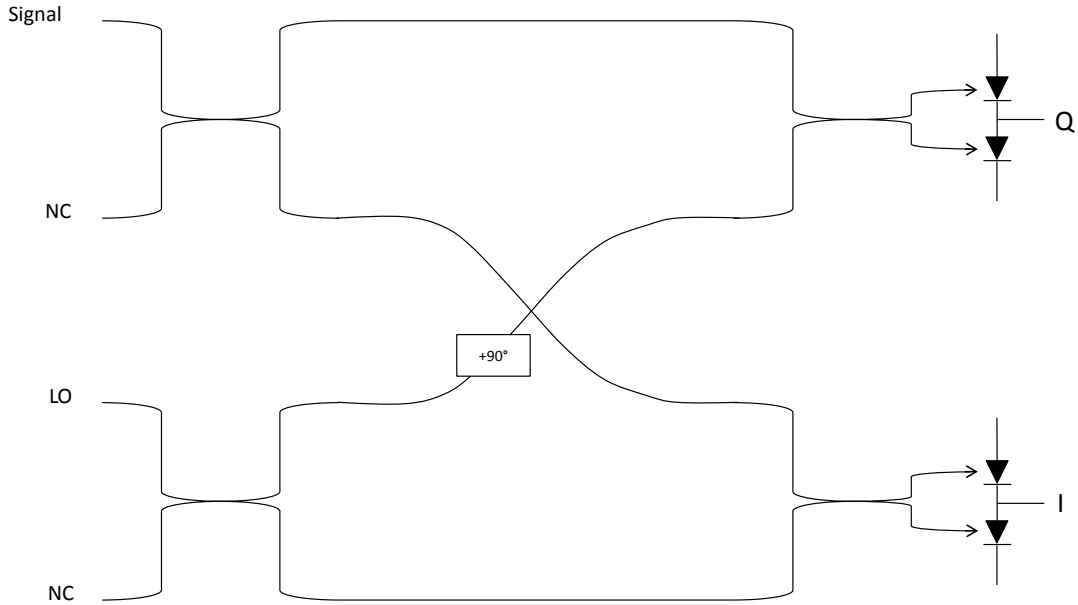
Figure 1. An Optical 90° Hybrid with differential detectors.

mixed with a local oscillator (LO) using a 90 degree optical hybrid as shown in Figure 1. The resulting I and Q signals are detected with differential detectors which subtract out the DC component and any systematic laser amplitude noise.

We can write the signal and LO as

$$A_s \exp(i(t\omega_s + \varphi_s)) \tag{2.1}$$

and

$$A_{lo} \exp(i(t\omega_{lo} + \varphi_{lo})) \tag{2.2}$$

where A_s and A_{lo}, ω_s and ω_{lo}, φ_s and φ_{lo} are the detected photon amplitude (α) in square root photons per symbol (i.e., in a digital communication system), frequency, and phase of the two signals and where t is time. The relationships between the amplitudes and the powers are

$$A_s = \sqrt{2P_s} \qquad A_{lo} = \sqrt{2P_{lo}} \tag{2.3}$$

The signal amplitude inputs and outputs for the second two splitters on the right in Figure 1 are shown in Figure 2 with the $\dfrac{\pi}{2}$ added to the LO signal in the top branch (Q branch).
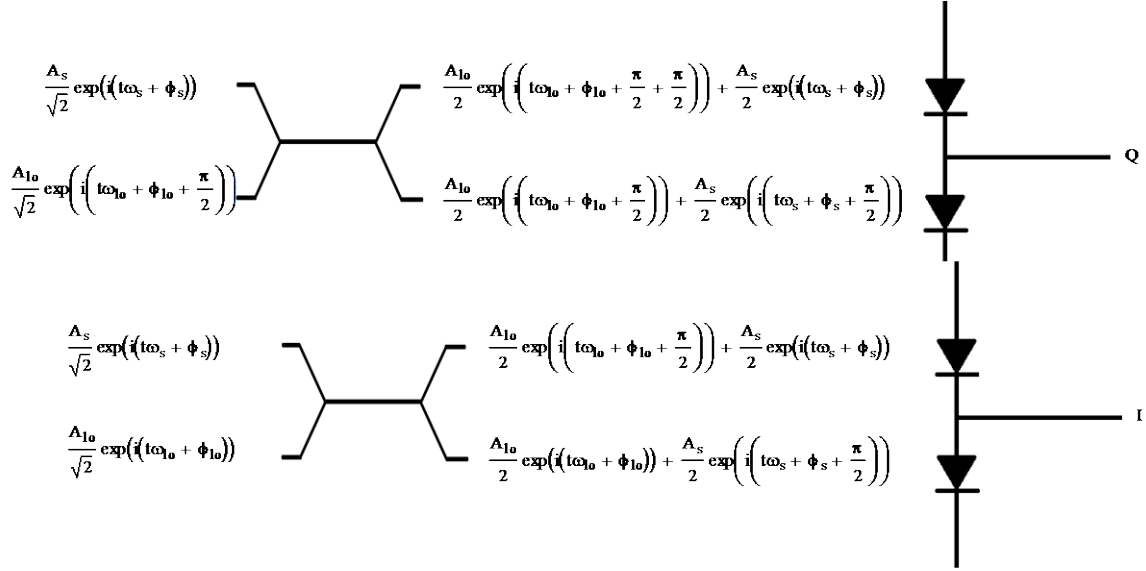
Figure 2 The final signals applied to the photodetectors.

Taking the real part of each of the four terms on the right, squaring, and subtracting the top two from each other and subtracting the bottom two from each other (because of the differential detection), we arrive at the detected signals for I and Q by extracting the frequency difference terms

$$I = \frac{1}{2} \cdot A_s \cdot A_{lo} \cdot \cos(\Delta\varphi + \Delta\omega t)$$

$$Q = \frac{1}{2} \cdot A_s \cdot A_{lo} \cdot \sin(\Delta\varphi + \Delta\omega t) \qquad (2.4a,b)$$

or

$$I = \sqrt{P_s \cdot P_{lo}} \cdot \cos(\Delta\varphi + \Delta\omega t)$$

$$Q = \sqrt{P_s \cdot P_{lo}} \cdot \sin(\Delta\varphi + \Delta\omega t) \qquad (2.5a,b)$$

where P_s and P_{lo} are the optical power of the signal and LO respectively, $\Delta\varphi$ is the relative phase of the applied signal and LO, and $\Delta\omega$ is the frequency difference between the signal and the LO.

A simulation was performed in MathCad starting with the four equations on the right of Figure 2. In each of the four time series the square of the real part of each time sample was taken to obtain the RF current amplitude (or, equivalently, modulated detected optical power) for that point in time in terms of detected photons per sample point. Each point was then "randomized" by assigning it a value by the MathCad Poisson generator to generate an ensemble for each of the four detector signals. P_s was set to 25 (the amplitude then is $\sqrt{2*25}$) detected photoelectrons and P_{lo} was set to 1 x 10^6 (the amplitude is $\sqrt{2*10^6}$) detected photoelectrons and the phase angle was set to 45 degrees. Each pair of resulting signals for the I and Q branches were subtracted to simulate the current subtraction in the differential detection diode circuit. A Fourier transform was performed on each of the resulting I and Q signals and

the value at the difference frequency for each was recorded. This was repeated 5000 times. Each of the resulting [I , Q] values is plotted below in Figure 3.
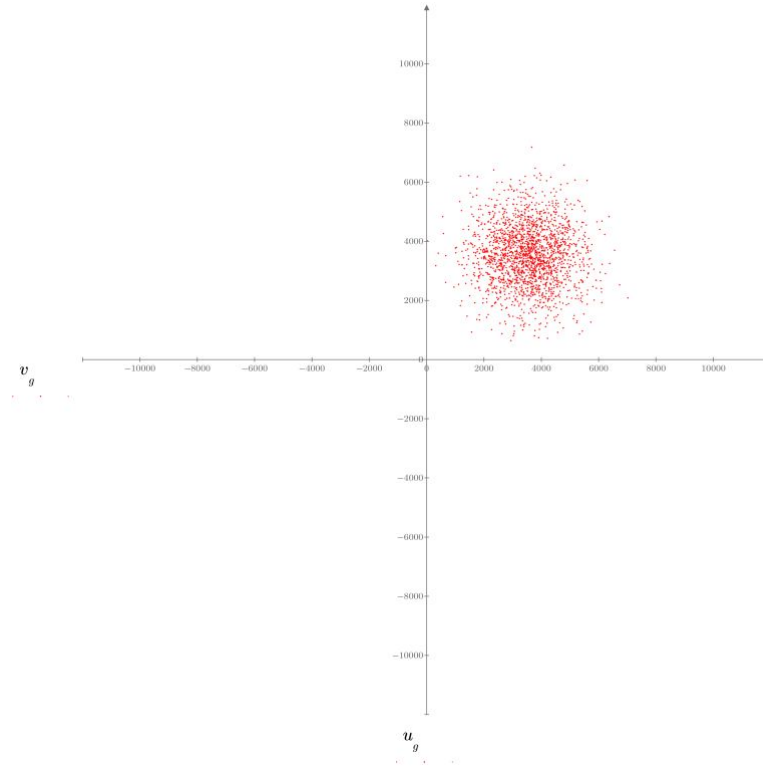
Figure 3. Heterodyne simulation of I (v_g) and Q (u_g) output of a 90 degree optical hybrid.

Since the 90 degree hybrid splits the signal into two, the I and Q branches each receive 25/2 signal photoelectrons and 10^6/2 LO photoelectrons combined. The expected signal in the I branch when the input signal is at a phase angle of 45 degrees and is

$$I = \sqrt{P_s \cdot P_{lo}}\cos(45)$$

$$I = \frac{1}{\sqrt{2}}\sqrt{25 \cdot 10\char94 6}$$

$$I = 3535.5 \tag{2.6}$$

And likewise for the Q branch

$$Q = \sqrt{P_s \cdot P_{lo}}\sin(45)$$

$$Q = \frac{1}{\sqrt{2}}\sqrt{25 \cdot 10\char94 6}$$

$$Q = 3535.5 \tag{2.7}$$

for a total vector length of

$$R = \sqrt{3535.5^2 + 3535.5^2} = 5000 \tag{2.8}$$

The The I and Q branch each receive $\sim \frac{LO}{2}$ and so have $\sqrt{\frac{LO}{2}}$ noise each. Added in quadrature the radial (amplitude) noise is $\sqrt{LO} = \sqrt{10^{\wedge}6} = 1000$. These calculations agree well with the simulation within the limits of the noise (Amplitude = 5003.0 photons /measurement, amplitude noise = 1000.1 rms photons /measurement) . The signal to noise ratio for a heterodyne detected signal of 25 detected photons using a 90 degree optical hybrid is $\sqrt{25}$ = 5 which also agrees well (5003.0/1000.1 $\cong$ 5.002) with the simulation results.

The results of simulation of magnitude and phase noise of the system as described was performed and is shown in Figure 4. This simulation was carried out in MathCad. The phase noise for the all optical full quadrature detection is

$$\varphi_{noise} = \frac{1}{\sqrt{n}} \qquad (2.9)$$

For n = 25 we should have a phase noise of 0.2 Radians. The simulation is in good agreement yielding 0.204 R.
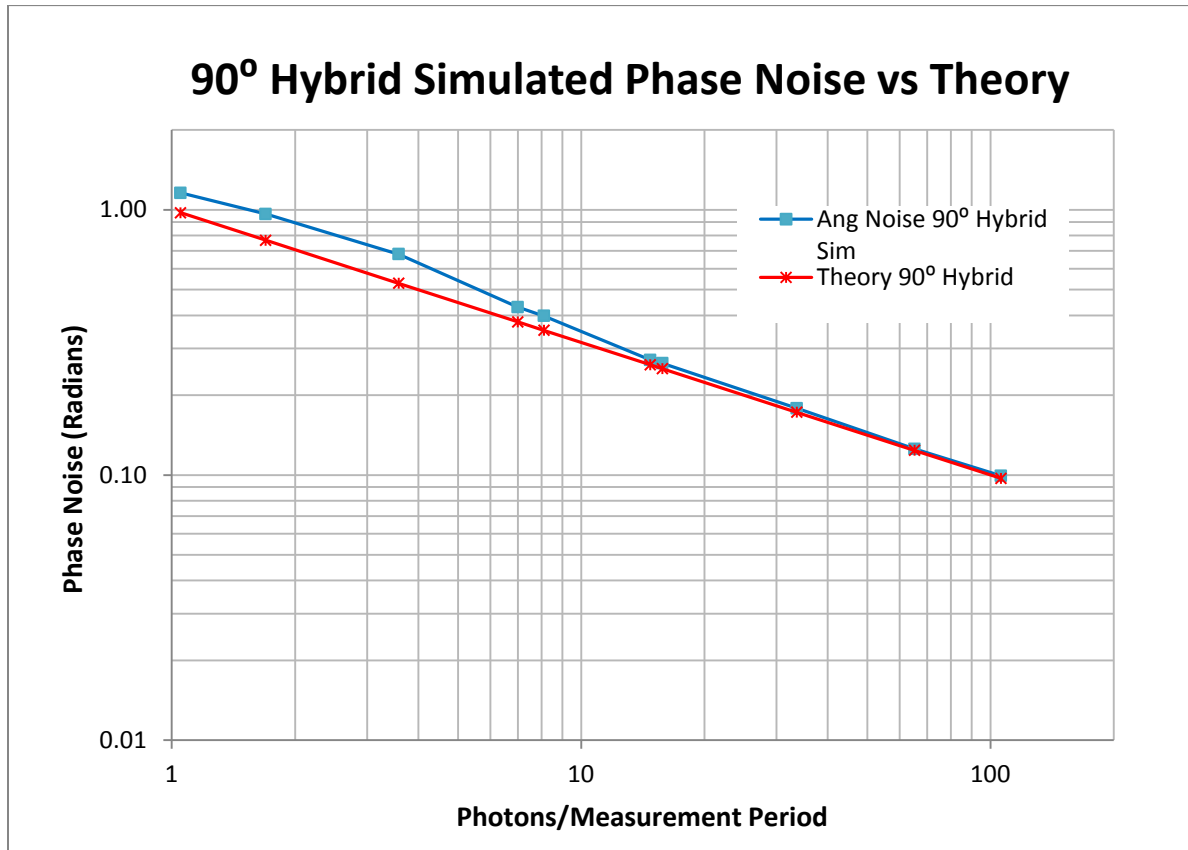
Figure 4. Simulation of phase noise in the heterodyne 90 hybrid system. The theoretical plot for $\varphi_{noise} = \frac{1}{\sqrt{n_\gamma}}$ where n_γ is the number of photons per measurement period.

Figure 4 plots theory and simulation of phase noise vs detected signal photons. The simulation is noticeably noisier than the theory for very low photon number (< 10) because at these low levels the signal amplitude is close to the IQ origin and outliers of the simulated measurements are in different quadrants than that of the centroid of the signal and in some cases there are simulated data points in all four quadrants as shown in figure 5. These outliers can then have deviations on the order of $\pi/2$ whereas the theory is derived from a small angle approximation that will not be accurate for angles greater than 0.1 radians.
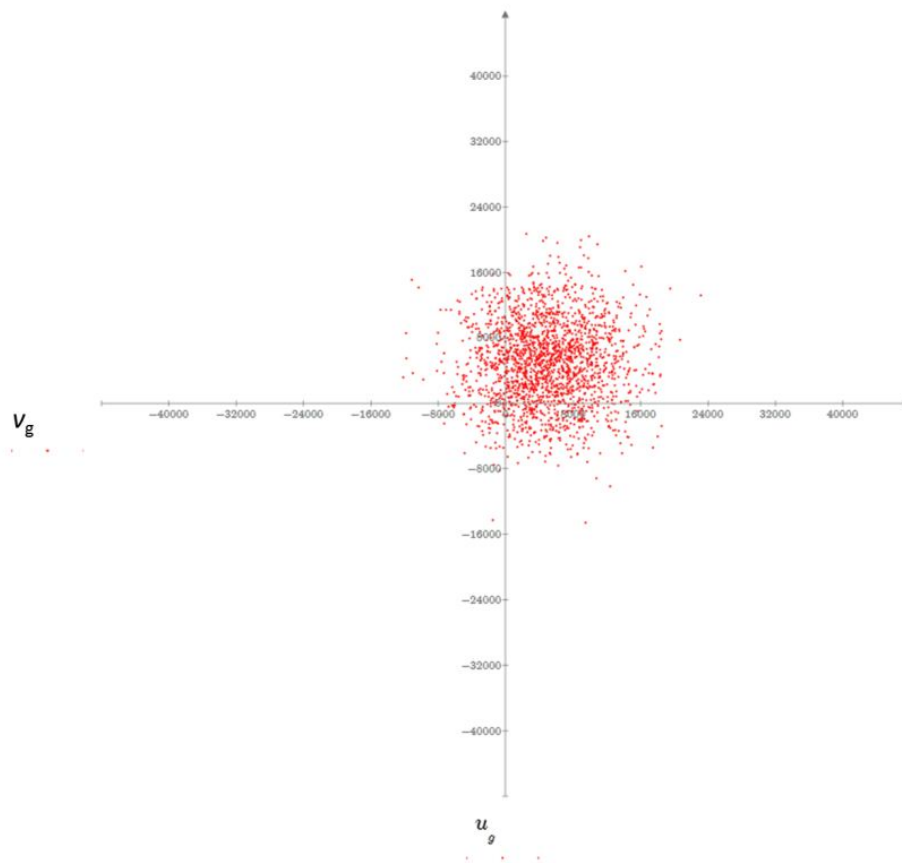
Figure 5. Here n = 2 (φ = 45 degrees) and the simulation results are in all four quadrants producing increased phase noise over the simplified theoretical model.

2.2   Initial measurements

Measurements have been made with a simplified system shown in Figure 6 in order to verify the basic heterodyne system and scaling factors such as fiber optic connector loss, 50/50 splitter loss, detector quantum efficiency, amplifier gain, and noise sources over and above photon shot noise. The signal and Local Oscillator are two independent lasers attenuated to about 15 milliwatts and 0.1 to 10 nanowatts. A polarization rotator is adjusted to align the linear and ellipsoidal components of the polarizations of the two lasers to maximize interference in the 50/50 splitter (180 degree hybrid). The heterodyne signal is differentially detected and fed to a low noise amplifier before being digitized by a Tektronix DPO73304D digital Oscilloscope at 100 Gigasamples/s. For these tests the frequency difference between the signal and LO lasers was 2.5 GHz and the scope lowpass filters were set at 4 GHz.
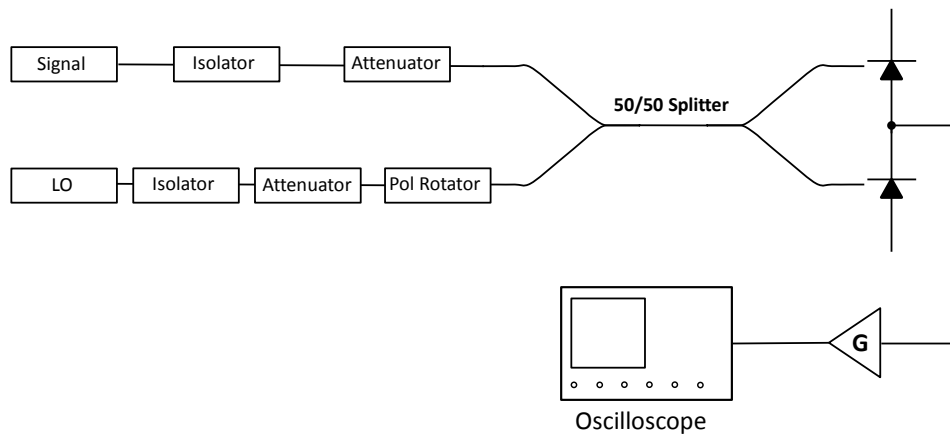
Figure 6 Simplified system for checkout
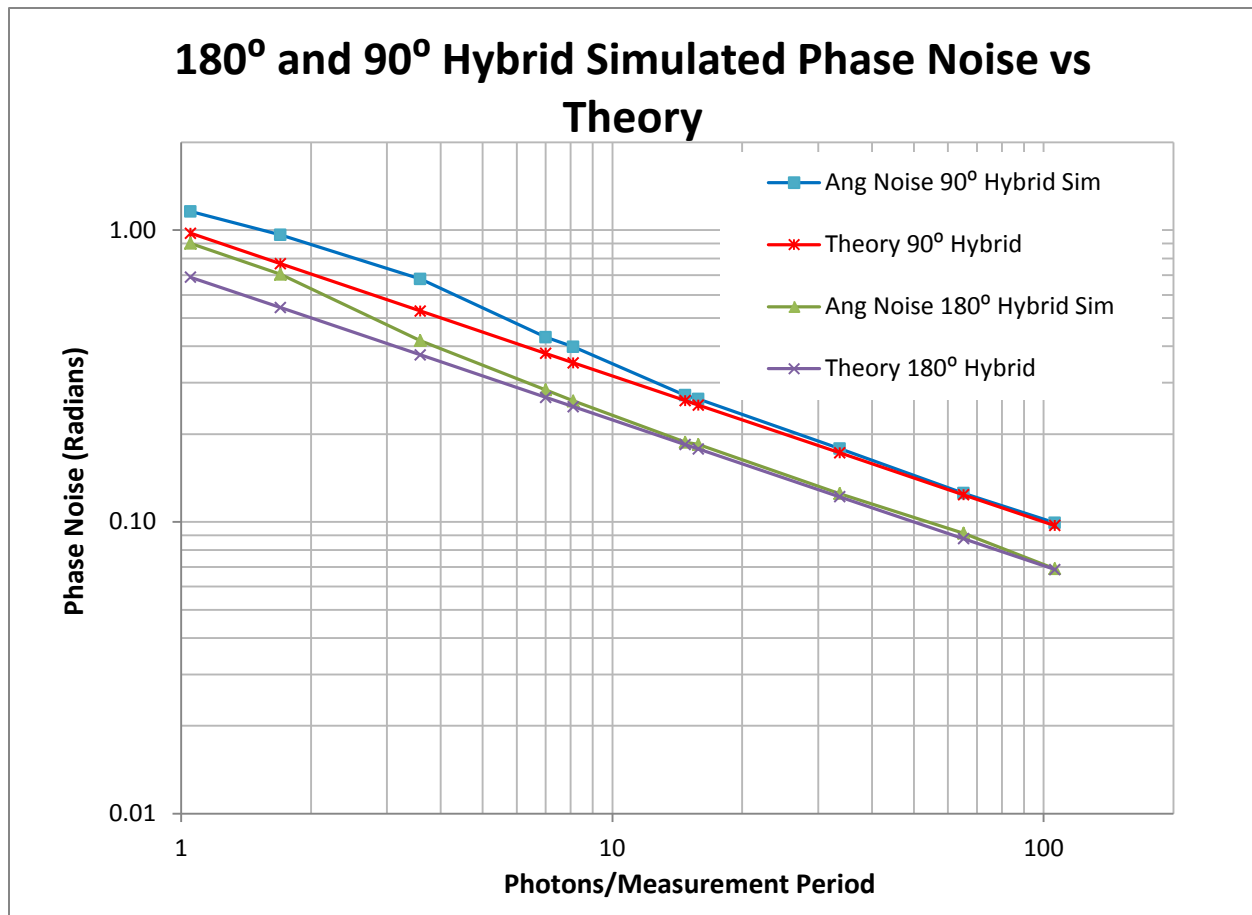
Figure 7. Simulated Phase Noise vs Theory for both the 180⁰ and the 90⁰ Hybrid

Figure 7 Shows the theoretical and simulated phase noise of the 180⁰ hybrid with the 90⁰ results included for comparison. The 180° hybrid has lower noise because it does not split the light signal between I and Q branches as in the 90° hybrid. With the 180° hybrid the I/Q processing is done numerically post detection after A/D conversion of the detected signal.
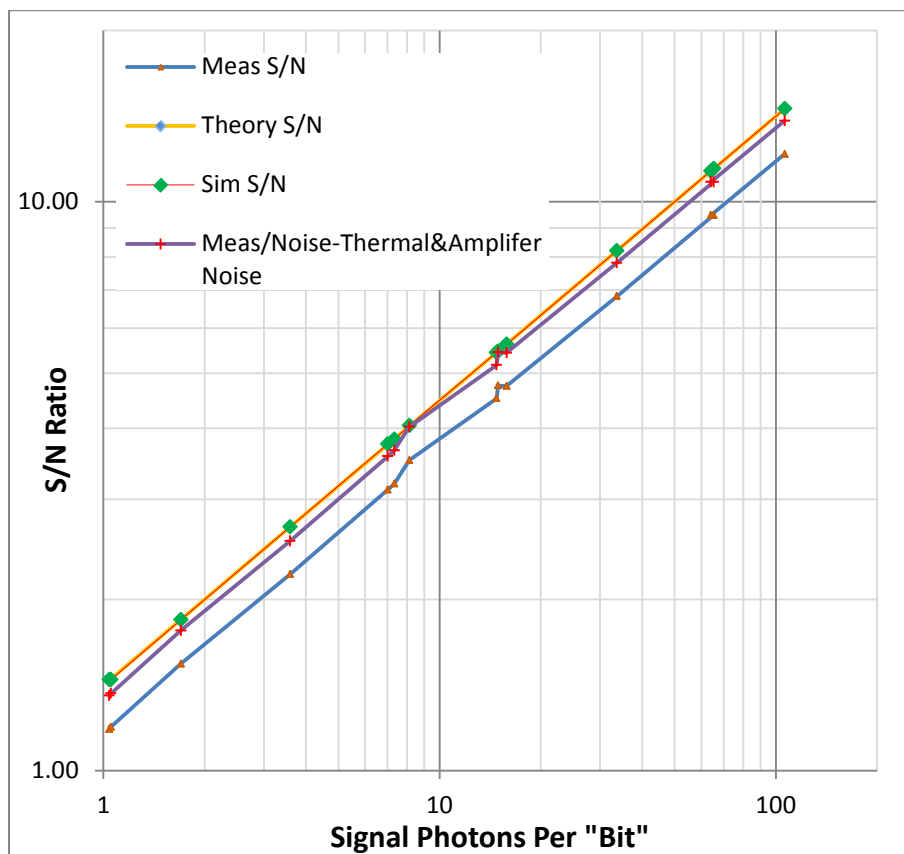
Figure 8. Basic heterodyne measurements with theory and simulation results.

Figure 8 plots the signal to noise of the measurements made with this system along with theoretical calculations and simulation results. All signal measurements are for detected photons (not incident photons).The simulation and theory are in complete agreement. The actual signal to noise measurements suffer from added thermal and amplifier noise and are about 17% less than the theoretical and simulation results. When the input lasers are turned off the thermal and amplifier noise is easily measured. When this noise is subtracted (in quadrature) from the measured signal only the photon shot noise should remain. The resulting S/N is only about 5% less than the theoretical and within measurement error limits.

2.3   Summary

Simulations of 90 and 180 degree hybrids were carried out and agree well with theoretical models. Measurement of 180 degree hybrid signal to noise ratios agree with theoretical and simulations within measurement error. In the coming months measurement of phase noise will be carried out on the 180 degree hybrid system to verify simulations.

3 Long-Wave Infrared (LWIR) Communications Development

(Mr. David Legare and Mr. David Hummel)

3.1 Introduction

The focus of this effort is on the evaluation of IR spectral region in the 8 to 14 micron wavelength range for improved free-space communications performance over legacy short wave IR (1.55 microns) in adverse atmospheric conditions including aerosol scattering and turbulence. Improved immunity to aerosol scattering and turbulence-induced scintillation at longer wavelengths has been theoretically modelled and experimentally verified in the past. However, the technology required to engineer a long range, high data rate, low SWAP communications system in the LWIR spectrum has only very recently become an emerging possibility. The initial phase of the effort described below entailed a set of experiments to measure relative performance over a short-range link through a homogenous atmosphere. The follow-on phase, currently on-going, will conduct long duration free-space atmospheric propagation measurement and performance evaluation under operational conditions over a 30 km link between AFRL-Rome and our Stockbridge test site. The ultimate program goal is to develop and evaluate a prototype LWIR system which represents a solution to an anticipated real operational requirement.

3.2 Background

Communications in the optical spectrum offers many advantages including low SWAP, extremely high bandwidth, and inherent covertness and jam-resistance due to spatial confinement of the radiated power to a very small free-space path volume. The latter also helps to minimize interference and spectral crowding in congested environments. Component technology covering most of the visible and IR spectrum is now already available, or at least reaching the point of foreseeable maturity, to provide practical implementations of compact, very high speed free-space communications links to support a number of applications. However, the physics of propagation through the lower atmosphere will always limit the utility of optical communications in this realm. Therefore, it only makes sense to fully investigate the use of that portion of the spectrum which is least susceptible to these detrimental effects.

Fortunately, as can be seen in an atmospheric transmission plot, figure 1, a number of windows t across the optical and IR spectrum exist which allow for low loss propagation in clear air conditions. Since the basic molecular composition of the atmosphere (minus water vapor) will always remain constant, these are the only usable portions of this spectrum that are of interest for all but very short range links. The essential issue then becomes energy loss via scattering from aerosols, mainly comprised of water, which are distributed along the propagation path. A less dominant, but still very significant loss mechanism is turbulence-induced scintillation. This will be investigated more thoroughly in the follow-on phase of the effort.

Atmospheric aerosols may be defined as any condensed particle of water, in a liquid or frozen state either falling through or suspended in the atmosphere. As such, these can include haze and fog, with particle sizes ranging from a fraction of a micron to 10 or more microns, up to fine mist, rain, snow, sleet and hail. Scattering is greatest when the wavelength of the signal is on the same order as the diameter

of the aerosol particle. The scattering mechanism is effectively the absorption and radiative redistribution of the signal energy in a pattern which is peaked in the direction of the signal entering the aerosol. When the particle sizes are very large compared to the wavelength, this scattering effect is minimal, and the main loss mechanism is simple absorption. Thus, in rain or snow, the losses at both the SWIR and LWIR are about the same. This is apparent in Figure 10 showing a plot of signal levels taken during a snow storm. Here it can be seen that the signal levels for both the SWIR and LWIR vary about equally with a change in precipitation rate. The rate of snowfall went from light to moderate, then back to light during the test period.
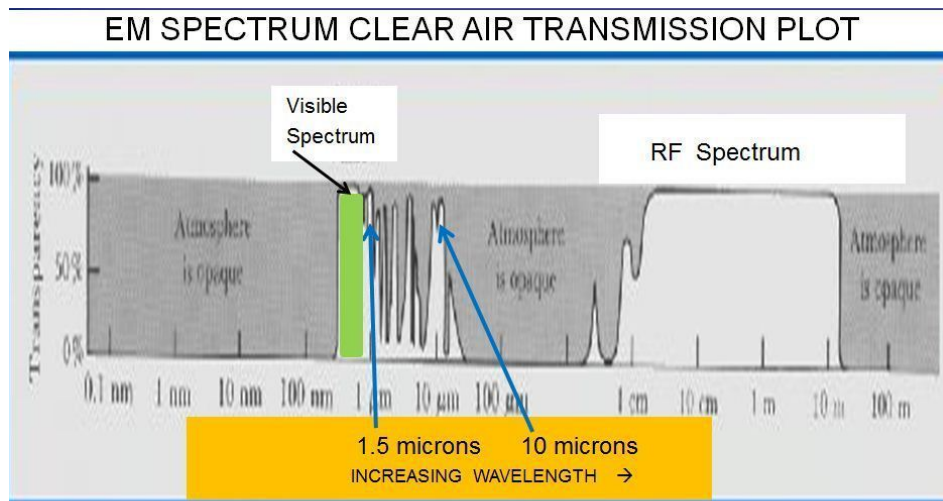
Figure 9. Clear air transmission plot.
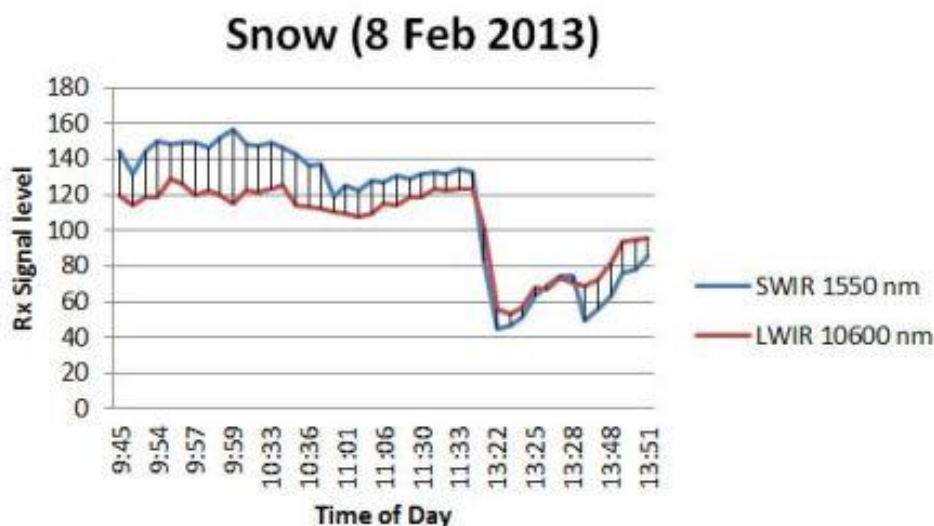
Figure 10. Attenuation with large aerosols (snow).

With the exception of clouds, which contain a very dense distribution of the full range of aerosol sizes, haze and fog are predominantly comprised of smaller particles, typically less than a few microns in diameter. Since it is extremely common for at least some fog or haze to be present along a portion of a signal path, it is reasonable to assume that operation in the LWIR spectrum could provide for improved information throughput and link availability compared to legacy SWIR systems. Even on apparently clear days, the atmosphere almost always contains a concentration of small aerosols that can significantly attenuate an optical signal, especially over long distances. So it can be seen that even a few tenths of a dB/km of signal loss due to these thinly distributed aerosols can have an appreciable effect over long range links of several 10's of kilometers. Therefore, although it makes sense to employ the SWIR spectrum for space and high altitude applications, there are some real advantages to utilizing the LWIR spectrum when any portion of the link transgresses the lower atmosphere.

Operation in the LWIR spectrum appears to provide the greatest advantage of overcoming adverse atmospheric effects, and needs to be thoroughly investigated for employment over long-range communications links. Although it is clear that no optical wavelength will operate under all conditions, the underlying assumption here is that the LWIR will perform markedly better (on the order of at least a few dB per km) under conditions of moderate atmospheric obscuration (haze, short patches of fog, etc.) which are present over at least some portion of a long path length a high percentage of the time. This makes the use of the optical spectrum more practical by allowing for a much higher system availability. The exact availability numbers are not yet known, as this analysis is part of the reason for conducting this program. However, it is assumed that they would show a significant improvement over legacy optical systems. The original link scenario considered for this program assumed current ISR downlink distances of around 10 to 30 Km. Distances of 100 miles or more might benefit even more due to the fact that, due to earth geometry, most of the path would occur in the upper atmosphere where aerosol concentration is low. However, even a small difference in attenuation over a very long distance could make or break the link. The Mie Scatter models and the literature suggests that there is an overall advantage to operating in the LWIR spectrum. What we are trying to do here is prove it out for ourselves experimentally.
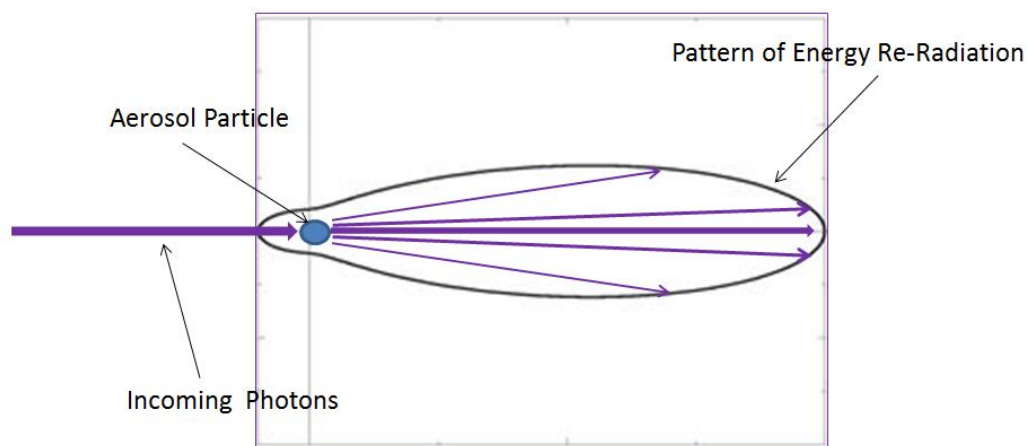
Figure 11. Radiation scattering phase function.

The major objectives of the program are to quantify the relationship between atmospheric parameters and signal attenuation, and to make a comparison between the performance of SWIR wavelengths (1.5 microns) and LWIR wavelengths (10.6 microns) under similar atmospheric conditions. Two key atmospheric attenuation mechanisms account for most of the transmission path loss in the IR spectrum.

These are Mie scattering and turbulence-induced scintillation. Mie scattering results from an interaction between the IR signal and aerosol particles such as those microscopic water droplets found in haze and fog. When the particle diameter is less than or approximately equal to the wavelength of the impinging photons, the energy is essentially redistributed in a pattern around the particle, with the bulk of it travelling forward in a cone of small angles off the main beam. This radiation pattern is defined as a phase function. An example phase function plot (for some given particle) is shown in Figure 11. Although most of the signal proceeds along its original path, a small portion is sent in other directions, with a resultant loss of power at the receiver.

The relationship between Mie scattering attenuation and aerosol parameters such as size distribution and concentration is fairly complex. The extinction coefficient α, given in equation (3.1), is not only a function of wavelength, but of physical properties of the individual aerosol particles. It is obvious from this expression that direct calculation of α for a given atmosphere would be a computationally intensive task, mainly due to the necessity of first having an accurate measure of the aerosol particle size distribution per unit volume $\frac{dN(r)}{d_r}$. Thus, the real problem in calculating attenuation using this formula is in obtaining the values of these atmospheric variables.

$$\alpha = \pi 10^5 \int_0^\infty Q_d\left(\frac{2\pi r}{\lambda}, n'\right)\left(\frac{dN}{dr}\right)r^2 dr \tag{3.1}$$

where α is the extinction coefficient in Km^{-1}, λ is the wavelength in microns, $\frac{dN(r)}{d_r}$ is the particle size distribution per unit volume (in cm^{-4}), n' is the real part of the refractive index of the aerosol, r, is the radius of a given particle size in cm, and $Q_d\left(\frac{2\pi r}{\lambda}, n'\right)$ is the scattering cross-section for a given aerosol type.

It is extremely difficult to measure aerosol particle size distributions and concentrations at any given point, and especially over a long distance where their values can vary dramatically in both time and space. The goal of the current program is not an attempt to make such measurements or to develop a scientific understanding of the physics of these scattering mechanisms. Rather, we correlate link performance with an easily obtainable atmospheric parameter that directly relates to the bulk effect of these aerosols along the transmission path. The Kruse model, discussed in the next section, provides an experimentally-verified expression for Mie scattering based on meteorological visibility V. As such, the extinction coefficient α can be expressed for any given wavelength λ as a function of a single variable V.

Although V is often determined crudely as the distance at which a human observer can discern a certain image (typically through haze or fog), it is quantitatively defined as the distance travelled by an optical beam before it is reduced to 5% of its original value. The current program will correlate experimentally-derived attenuation of simultaneously transmitted SWIR and LWIR signals over a folded path at near ground level with observed measures of atmospheric visibility. Visibility estimates used to date have been based on a combination of on-line reported values taken from the local area, as well as direct human observation. These results will also be correlated with values derived from the Kruse model. This will provide an additional level of confidence in the validity of the experiment, assuming the empirical and theoretical results are in agreement. It will also serve to verify the utility of the Kruse model for extension into the IR portion of the spectrum, since it was primarily derived from data collected in the visible portion of the optical spectrum. Note that although the results reported here were made based on the methods mentioned previously, we have since obtained an actual visibility meter, Figure 12, which will be available for use in future data collection. This device works on the principle of off-axis

scattering (particle phase function) between an optical emitter and detector separated by a few feet. The values provided would be accurate for our purposes assuming that the visibility measured over this short distance is uniform over the entire transmission path. It is safe to assume that this is the case for our .78Km link.

Figures 13-16 are images of visibility used to estimate V for data taken during the experiment. Figures 13 and 14 are a view looking West from the shelter housing the experiment transceiver. The distance to the far horizon in this view is about 1 Km. Figure 13 is the view under clear sky conditions. In Figure 14, it can be seen that the most distant tree line is mostly obscured. This image therefore corresponds to a visibility value V of about 1 Km. A similar comparison can be seen in the two views shown in figures 15 and 16. These are views looking East from the same shelter. With figure 15 as the clear sky view, and figure 16 likewise reveals an obscured tree line at the horizon, a distance of about 2 Km from the shelter. Other values of V for the purposes of the experiment were based on visual estimates using these two as a reference.

Figure 12. Visiometer deployed on the shelter.

Figure 13. Clear sky visibility

Figure 14. Overcast sky visibility

Figure 15. Clear sky visibility

Figure 16. Overcast sky visibility

3.3 Tasking

This report describes the initial (baseline) effort to conduct atmospheric propagation testing to evaluate the comparative performance of the LWIR spectrum (at around 10.6 microns) and the SWIR spectrum (at around 1.5 microns) under a range of atmospheric conditions including rain, snow, fog, and haze. The test-bed was established over a horizontal short-range folded path comprised of a retro-reflector placed 1300 feet away from the transceiver hardware to provide for a total path length of about .78 Km. The homogeneity of the atmosphere over this short range provided for a more accurate correlation between the observed visibility parameter V and the measured signal values propagating through this well-characterized atmospheric volume. A diagram of the transceiver hardware is shown below in Figure 17.
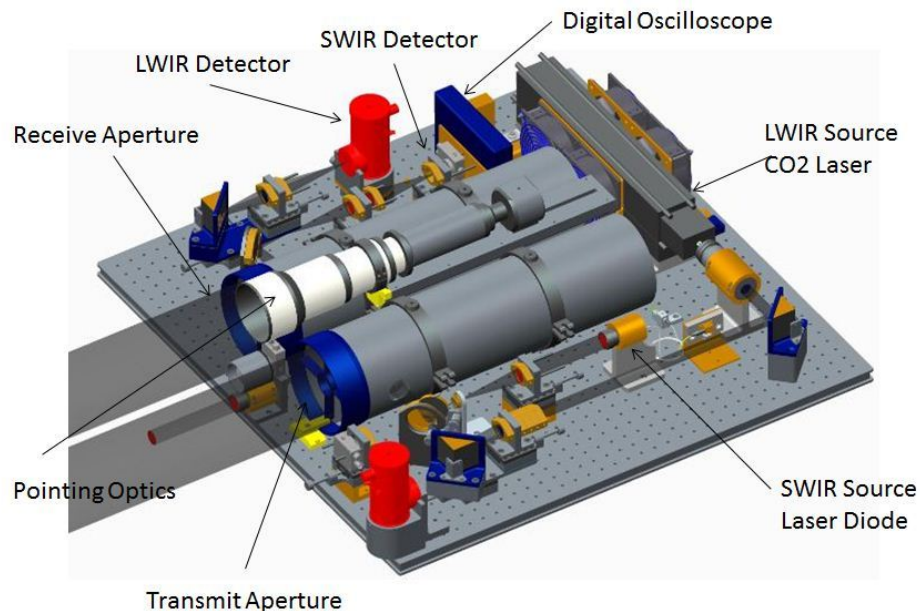
Figure 17. Diagram of optical transceiver assembly

3.4 Theoretical Model

A link budget model was developed to theoretically characterize the propagation for both the LWIR and SWIR signals. Equation (3.2) is the power received from the transmitter. The model can essentially be broken down into three major loss factors: 1) Free space path loss, 2) Losses due to aerosol scattering, and 3) System losses. Variables entering into the link budget calculation are listed in Tables 2 and 3 The scatter loss portion was based on the Kruse model, which calculates the extinction coefficient, α, as shown in equation (3.3).

Figure 18 is a plot of the of the link budget calculated for the .78 Km test link used in the experiment. Note that the system parameters entered for the model were tailored so that both the SWIR and LWIR signals would have the same received power at maximum visibility, where losses due to scattering were nil. Thus, since equal aperture sizes and transmitted power levels at both wavelengths would minimize

geometric losses (free space path loss) for the SWIR signal, these values were reduced for the SWIR so that only the comparative losses due to scattering would be apparent.

$$P_r = P_t\,\tau_t\tau_r\left(\frac{d_t D}{\lambda L}\right)^2 10^{-\frac{\alpha L}{10}} \tag{3.2}$$

$$\alpha = (4.434)\frac{3.91}{V}\left(\frac{\lambda}{550}\right)^{-q} \tag{3.3}$$

Table 2 Extinction Exponents vs Visibility

Visibility V	V > 50	6 < V < 50	1 < V < 6	0.5 < V < 1	V < 0.5
q	1.6	1.3	0.16 V+ 0.34	V - .5	0

Table 3 Link Budget Parameters

D = Rx Aperture Diameter (m)	d_t = Tx Aperture Diameter (m)
L= Path Length (m)	λ = Wavelength (m)
T_t= Tx System Loss	T_r = Rx System Loss

.78 Km Range Link Budget

Visibility (km)	λ 1550nm	Visibility (km)	λ 10600nm
0.8	-11.8851	0.8	-5.75859
0.9	-10.5765	0.9	-5.11432
1	-9.53184	1	-4.60615
1.1	-8.67914	1.1	-4.19664
1.2	-7.97037	1.2	-3.86088
1.3	-7.37229	1.3	-3.5816
1.4	-6.86116	1.4	-3.3465
1.5	-6.41956	1.5	-3.14655
1.7	-5.69579	1.7	-2.82669
1.9	-5.12854	1.9	-2.58462
2	-4.8889	2	-2.48517
2.2	-4.47752	2.2	-2.31918
2.5	-3.98928	2.5	-2.13154
3	-3.40392	3	-1.9242
4	-2.70124	4	-1.71193
5	-2.30663	5	-1.61857
6	-2.0626	6	-1.57397
6.5	-1.97448	6.5	-1.5609
7	-1.90213	7	-1.55153
7.5	-1.84216	7.5	-1.54476
8	-1.79204	8	-1.53984
9	-1.71414	9	-1.53358
10	-1.65771	10	-1.53018
12	-1.5849	12	-1.52723
14	-1.54321	14	-1.5263
16	-1.51841	16	-1.52599
18	-1.50325	18	-1.52588
20	-1.49379	20	-1.52585

Figure 18. Comparative link budgets: SWIR vs LWIR

3.5 Method of Data Collection

The purpose of this first phase of the LWIR in-house program was to accurately characterize atmospheric propagation loss due to aerosol scattering simultaneously at both the SWIR (1.55 μ) and the LW IR (10.6 μ). The desired result was to quantify both the relative performance of the two wavelengths, and the absolute performance of the longer IR wavelengths for the purpose of ultimately designing an "all weather" optical communications system that could be deployed in an operational environment.

The aerosol scatter loss measurements will were made over a folded path using a 5" diameter first-surface, gold-coated retro-reflector about 1300 feet from the transmitter/receiver system for a total distance of about .78 Km. The transmitter/receiver assembly consisted of a 3'x3' optical breadboard containing the optical and electro-optic hardware, along with the control and measurement electronics and software required to generate both of the test wavelengths. The test system was mounted on a precision pointing gimbal and co-aligned with a high resolution telephoto camera so that it could be precisely bore-sighted on the retro-reflector at the far end of the propagation path. Measurements were taken at all possible opportunities under a wide range of atmospheric conditions to include clear air (maximum visibility) and fog/haze, rain and snow. The test range was located at the AFRL/Rome site and conducted along a horizontal ground level path. The transmitter/receiver system was operated from inside an environmentally-controlled military field shelter (through an open door), so that it could be conveniently protected while experiments were conducted under adverse weather conditions. The shelter was located in the Satcom test area on the South side of Building 3 at AFRL/RI, in Rome, NY. The other end of the folded path was located at the far southwest end of the building 3 parking lot, about 1300 feet away. The retro-reflector was positioned on a 20' tower attached to our HMMWV at this point.

Both the SWIR (1.55 μ) and LWIR (10.6 μ) signals were generated simultaneously at a 5 KHz pulse rate and emitted along a parallel path from the transmit side of the test system. The signals returned from the retro-reflector were collected into a 5" aperture telescope which was mounted next to, and aligned with the transmit aperture. The output of the receive telescope proceeds through a beam splitter to separate the two wavelengths into separate paths for subsequent beam shaping, optical filtering and detection. The detector outputs were fed to separate channels of an oscilloscope which was programmed to average the peak amplitudes of each pulse (in millivolts) in the train with about 30 seconds of averaged pulses comprising each data point. A number of these data points, taken over a typical period of several minutes to an hour during which the atmospheric conditions (ie fog/haze density) remained relatively constant, were then averaged to provide a single value for received power corresponding to the observed value of constant atmospheric visibility during that time period. These values represent the expected received power levels for that given atmospheric condition, and subsequently were used to calculate an aerosol extinction loss for each wavelength in dB as:

$$ \text{LExt} = 10 \, \text{Log} \left(\frac{\text{PR}}{\text{PT}} \right) - 10 \, \text{Log} \left(\frac{\text{PR}_{\text{cal}}}{\text{PT}_{\text{cal}}} \right) \tag{3.4} $$

Where: PT, PR = Transmit, Receive Power for a given test during non-clear air conditions, and PTcal, PRcal = Transmit, Receive power measured during a clear air (maximum visibility; no aerosol scattering loss) test. The latter was used as a calibration value which essentially provides a measure of the combined transmitter/receiver *system loss* and *free-space path loss*. Therefore, the second term of LExt represents the combined fixed test system loss plus the total clear air path loss, both of which should never change. Thus, this serves as a reference from which to derive the actual value of just the scatter

extinction loss for any given atmospheric condition. Since the atmospheric path length is fixed at .78 Km, the extinction loss for the given atmospheric test can be easily expressed in standard form as:

$$\text{Aerosol Extinction Loss} = \text{LExt}/.78 \ \text{dB/Km} \qquad (3.5)$$

Note that PT and PTcal values used in the calculation were measured as small signals scattered off a beam splitter in the transmitter chain in real time, and therefore were only a small unknown fixed fraction of the total transmitted power. This still makes for a valid calculation since the ratio of this measured power to actual total transmitted power is unimportant, as long as the ratio remains constant throughout the test. Thus, the laser sources were controlled so that these PT and PTcal values were kept constant throughout all of the experiments.

Also note that the signal transmit power levels for both lasers were adjusted so that the receive power for each wavelength was close to equal under clear air conditions. Although this wasn't necessary to make the actual loss measurements (since the loss at each wavelength is calculated as a ratio between its own transmit and receive value), it allows for a more direct comparison of the data for each wavelength.

3.6   Data Collected

Due to initial problems with the experiment hardware and the inability to continue the data collection effort beyond August 3013, it was only possible to obtain a few good data sets during this first phase of the effort. The first of these shown in Table 4 below were taken over a series of three clear air days where the atmospheric visibility was known to be at a maximum. The results from each of these days were averaged together to provide a best value for PRCal at each wavelength. The reference values, shown as 287 mv (for λ = 1550 nm) and 307 mv (for λ = 10600nm) are used hereinafter to calculate the extinction loss LExt for data taken at other (lower) values of atmospheric visibility shown in Tables 5, 3.15, and 3.6. It can be readily seen that they are well in agreement with the results predicted by the Kruse model. What is particularly interesting is the very close correlation between the comparative path loss values (Δ dB/Km) derived from the empirical data and what is predicted by the model in figure 15. Thus, though less than the originally desired amount of data was taken, it agrees extremely well with the predicted results. This leads to a very high level of confidence in the Kruse model for use as a predictor of atmospheric aerosol extinction for the entire IR spectral band of interest, at least for visibility ranges of around one Km to clear air conditions. This is particularly encouraging since this simple model is based solely on the parameter V (atmospheric visibility), as long as the aerosols are essentially microscopic in size (not rain or snow). Note from the previous background discussion (and figure 10) that the primary effect of these larger particles is absorption (not scattering), and that they have an essentially equal effect on all wavelengths of interest.

Although we are now in the second phase of the effort which involves data collection over the 30 Km Griffiss-Stockbridge link, we plan to re-establish and collect additional data on the .78 Km link to further characterize and validate these assumptions, and perhaps provide enhancements to the Kruse model based on observed propagation results in the IR spectrum.

Table 4 Clear Air Data (for measurement calibration)

Maximum Visibility Days	23 April		25 April		April 17				
	1550 nm Rx	10600 nm Rx	1550 nm Rx	10600 nm Rx	1550 nm Rx	10600 nm Rx			
	256.08	300.1	248.27	250.1	358.3	327.8			
	257.73	328.1	250.58	231.3	333.8	320.9		Reference Clear Air Values	
	237.82	285.1	267.96	234.9	362.4	312.9			
	241.34	314.8	283.96	244.2	332.4	311.1			
	260.37	326.3	290.29	240.5	342.9	270			
Data Points	253.11	322.3	284.35	234.2	285.1	247		1550 nm	10600 nm
	261.14	328.3	323.73	246.9	351.3	368			
	249.04	297.1	284.57	249.2	334	370.2		287	307
	257.84	232.3	259.82	255.3	286.8	301			
	239.58	308.9	285.89	275	285.9	317.8			
	251.02	276.6	290.07	282.2	288	312			
	260.48	302.7	285.23	297.3	276.6	287.3			
	230.12	295.5	281.82	286.3	287.1	288.9			
	248.16	304.7	304.15	296.9	352.1	389.5			
	245.19	305.9	286.99	295.5	312	335.6			
	239.47	309.2	301.18	316.9	291	314			
	242.55	312.1	266.75	337.7	299	290			
	259.38	300.4	267.85	329.6	279.3	286.5			
			267.52	323.1	299.4	296			
Averages	249.47	306.13	330.44	342.9	275.5	319.8			
			316.58	331.7	263.5	283.6			
			325.27	310.2	289.8	306.1			
			357.83	317.8	286.4	307.6			
			334.84	357.4	274.2	325.1			
			363.55	360.4	268.4	275.1			
			339.68	293.4	270.6	290.3			
			296.01	335.6	262.6	294.3			
			310.75	344.4	324.9	319.8			
			299.42	342.8	330.6	303.6			
			309.54	324.8	371.7	309.2			
			289.85	312.1	398.7	331.3			
			330.66	332.1	377.3	349.6			
			318.01	352.9	294.7	315.9			
			310.86	374.1	335.6	300.8			
			305.58	304.9	339.9	297.5			
			307.56	364.2					
			312.84	323.8	312.05	310.75			
			283.36	296.4					
			293.86	328.1					
			285.34	322.5					
			282.92	290.7					
			298.73	304.64					

Table 5 Data at 3 Km Visibility (5/10/13)   Table 6 Data at 1 Km Visibility (8/30/13)

10 May 2013

Time	1.55 Rx	10.6 Rx
16:15	167.97	262
16:19	185.9	286.7
16:21	197.34	257.8
16:22	189.53	247.8
16:24	173.36	255.6
16:26	157.19	270.7
16:28	167.2	285.2
16:29	182.27	289.3
Average	178	269

General Atmospheric Conditions

Light rain
Light haze
Est Visibility: 3 Km

1550nm
Path Loss Due to Scattering
Measured: (dB/km) = -2.66
Kruse Model (Vis: 3 Km) = -2.42

10600nm
Path Loss Due to Scattering
Measured: (dB/Km) = -.74
Kruse Model (Vis: 3 Km) = -.50

Comparative Path Loss Δ (dB/Km)
Measured: 1.92
Kruse Model: 1.92

30 Aug 2013

Time	1.55 Rx	10.6 Rx
8:55	19.811	106
8:57	18.414	104.6
9:00	15.246	104.2
9:03	31.559	111.8
9:04	34.903	116
9:06	45.353	122.4
9:07	49.852	126.1
9:08	44.913	126.9
9:09	40.546	119.6
9:10	39.721	117.7
	34.0318	115.53
Average	34	116

General Atmospheric Conditions

Light mist
Moderate Fog
Est Visibility: 1.0 Km

1550nm
Path Loss Due to Scattering
Measured: (dB/km) = -11.87
Kruse Model (Vis: 1.0 Km) = -10.13

10600nm
Path Loss Due to Scattering
Measured: (dB/km) = -5.42
Kruse Model (Vis: 1.0 Km) = -3.9

Comparative Path Loss Δ (dB/Km)
Measured: 6.45
Kruse Model: 6.23

Table 7 Data at 3 Km Visibility (5/23/13)

23 May 2013

Time	1.55 Rx	10.6 Rx
9:01	159.72	258.4
9:02	167.09	255.9
9:04	177.32	260.5
9:08	156.31	245.6
9:20	189.64	245.2
9:22	164.78	232.2
9:24	155.76	250.5
9:27	149.71	274.3
9:28	151.14	275.8
9:30	159.61	260.4
9:32	173.91	265.1
9:37	171.38	284.3
9:38	166.1	285.3
9:40	170.5	282.7
9:46	187.55	284.2
10:01	194.48	293
10:10	170.5	285.7
10:35	236.61	326.2
10:37	225.72	348.5
10:54	191.62	334.1
Average	176	277

General Atmospheric Conditions

Light rain
Light haze
Est Visibility: 3 Km

1550nm
Path Loss Due to Scattering
Measured: (dB/km) = -2.72
Kruse Model (Vis: 3 Km) = -2.42

10600nm
Path Loss Due to Scattering
Measured: (dB/Km) = -.57

Comparative Path Loss Δ (dB/Km)
Measured: 2.15
Kruse Model: 1.92

3.7 Analysis/Conclusions

3.7.1 SWIR

There are many considerations in designing an atmospheric optical communications link. An obvious advantage of legacy SWIR (1.5 µ) communications is about a 16dB margin in geometric space path loss (due to higher gain resulting from a higher optical frequency) over the LWIR (at 10.6 µ) for the same size transmit/receive aperture. However, the resulting narrower beam-width also makes pointing more difficult due the required increase in pointing accuracy, and the random beam wander resulting from turbulence-induced scintillation. These scintillation effects also introduce jitter on the received signal in the detector focal plane, which can further result in an average signal degradation, and lowered signal to noise ratio. Longer optical wavelengths are much less susceptible to all of these scintillation effects, and thus have a countering advantage which may overcome at least some, if not all of the obvious geometric path loss advantages of an SWIR system. These effects will be investigated further in the next phase of the effort using data collected over the 30 Km Griffiss-Stockbridge link. The purpose of the present analysis is to quantify the effects of aerosol scattering. The data collected showed a good correlation with the Kruse model for visibilities ranging from around 1 Km to clear air conditions. This model will now be used to predict the comparative performance of the SWIR and LWIR wavelengths over a hypothetical 50 Km link.

Figure 19 shows the effects of scattering alone. In this case, the transmit and receive aperture sizes were selected such that the link margins would be equal at very high visibility, where the scattering losses were nil. For comparison, in figure 20, the model was run with equal aperture sizes for both wavelengths to more fully illustrate all components of the link budget. Here, the 16dB SWIR margin becomes apparent as the plot approaches 100% percent atmospheric visibility, and the scattering loss becomes negligible. Figure 21 further illustrates a case nearly optimized for the LWIR in which the 10.6 µ wavelength operates with an aperture of twice the diameter of the SWIR to close the gap in the geometric path loss advantage. Though doubling may at first seem like a considerable change, it is seen that it is only an increase from 5 cm to 10 cm (about 2" to 4").

All else being equal, it is clear from figure 21. that the LWIR has a performance advantage where the average visibility over the link is less than about 15 Km. We know from our own experience that it is very difficult to differentiate visibility levels beyond about 6 to 7 kilometers from clear air conditions purely by sight. Therefore, it would be equally difficult to estimate the percentage of time that the link would experience average visibility conditions exceeding this 15 Km threshold without taking actual long term data measurements. This will be done in the next phase of the effort.

Thus, a major goal in this next phase will be to quantify the atmospheric statistics that would relate to the availability of an operation link over a significant path length of at least a few tens of kilometers. A distinguishing feature of longer links is the variability of the atmospheric parameters, including visibility, along the path. Note that the data collected in the present phase was over a relatively short (.78 km) folded path over which the atmospheric conditions could be assumed to be homogenous. Ultimately, it would be desirable to express the varying visibility over a much longer path as a single value of equivalent (or average) visibility which could be correlated with the Kruse model. Values for link availability could then be derived as a function of the atmospheric statistics along the path.

Data collection will take place over the wide range of seasonal atmospheric conditions that normally occur in the Central New York area. The results provided by the Griffiss-Stockbridge test-bed could therefore support a first-order prediction of SWIR and LWIR absolute and comparative performance for a variety of anticipated user applications in a wide range of global operating environments.
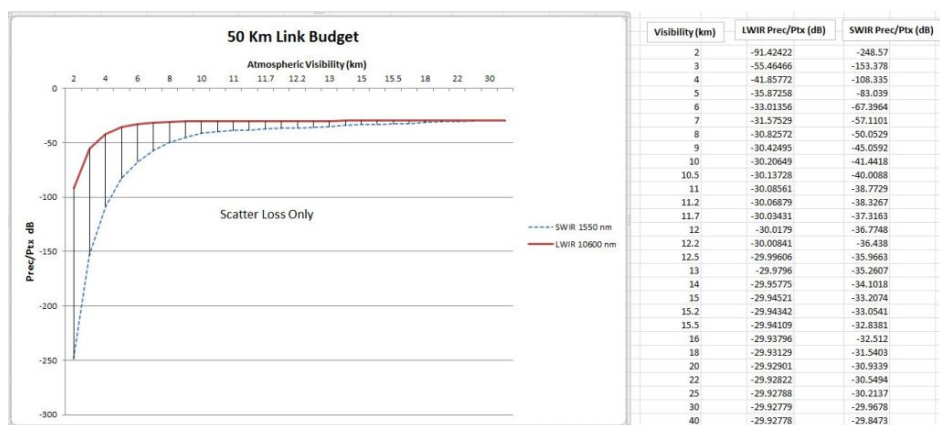
Figure 19- Scatter Loss Only

| Visibility (km)	LWIR Prec/Ptx (dB)	SWIR Prec/Ptx (dB)
2	-91.42422	-248.57
3	-55.46466	-153.378
4	-41.85772	-108.335
5	-35.87258	-83.039
6	-33.01356	-67.3964
7	-31.57529	-57.1101
8	-30.82572	-50.0529
9	-30.42495	-45.0592
10	-30.20649	-41.4418
10.5	-30.13728	-40.0088
11	-30.08561	-38.7729
11.2	-30.06879	-38.3267
11.7	-30.03431	-37.3163
12	-30.0179	-36.7748
12.2	-30.00841	-36.438
12.5	-29.99606	-35.9663
13	-29.9796	-35.2607
14	-29.95775	-34.1018
15	-29.94521	-33.2074
15.2	-29.94342	-33.0541
15.5	-29.94109	-32.8381
16	-29.93796	-32.512
18	-29.93129	-31.5403
20	-29.92901	-30.9339
22	-29.92822	-30.5494
25	-29.92788	-30.2137
30	-29.92779	-29.9678
40	-29.92778	-29.8473

Figure 20 - Equal Aperture Size

Visibility (km)	LWIR Prec/Ptx (dB)	SWIR Prec/Ptx (dB)
2	-108.0232	-248.57
3	-72.06359	-153.378
4	-58.45665	-108.335
5	-52.47152	-83.039
6	-49.6125	-67.3964
7	-48.17422	-57.1101
8	-47.42465	-50.0529
9	-47.02388	-45.0592
10	-46.80543	-41.4418
10.5	-46.73621	-40.0088
11	-46.68454	-38.7729
11.2	-46.66772	-38.3267
11.7	-46.63324	-37.3163
12	-46.61683	-36.7748
12.2	-46.60735	-36.438
12.5	-46.59499	-35.9663
13	-46.57853	-35.2607
14	-46.55669	-34.1018
15	-46.54414	-33.2074
15.2	-46.54236	-33.0541
15.5	-46.54002	-32.8381
16	-46.53689	-32.512
18	-46.53023	-31.5403
20	-46.52794	-30.9339
22	-46.52715	-30.5494
25	-46.52681	-30.2137
30	-46.52672	-29.9678
40	-46.52672	-29.8473

Figure 21 - Larger LWIR Aperture

Visibility (km)	LWIR Prec/Ptx (dB)	SWIR Prec/Ptx (dB)
2	-95.98196	-248.57
3	-60.02239	-153.378
4	-46.41545	-108.335
5	-40.43032	-83.039
6	-37.5713	-67.3964
7	-36.13302	-57.1101
8	-35.38345	-50.0529
9	-34.98268	-45.0592
10	-34.76423	-41.4418
10.5	-34.69501	-40.0088
11	-34.64334	-38.7729
11.2	-34.62652	-38.3267
11.7	-34.59205	-37.3163
12	-34.57563	-36.7748
12.2	-34.56615	-36.438
12.5	-34.55379	-35.9663
13	-34.53733	-35.2607
14	-34.51549	-34.1018
15	-34.50294	-33.2074
15.2	-34.50116	-33.0541
15.5	-34.49882	-32.8381
16	-34.49569	-32.512
18	-34.48903	-31.5403
20	-34.48674	-30.9339
22	-34.48595	-30.5494
25	-34.48561	-30.2137
30	-34.48552	-29.9678
40	-34.48552	

3.7.2 MWIR to LWIR Band

The simple Kruse model has been demonstrated to be a reasonably accurate predictor of scattering performance in the LWIR band (around 10.6 microns) and the SWIR band (around 1.5 microns). It would thus be safe to assume that this model could be used to estimate comparative performance of wavelengths between these extremes, assuming that they are also within a clear-air transmission window. Such conditions exist for the spectral regions of approximately 3 to 4.1, 4.3 to 5, 5 to 5.1, and 7.7 to 8.5 microns.

Besides the obvious advantage of higher signal gain for a given size optical aperture, operation at these intermediate wavelengths also has a potential advantage in the implementation of the receiver. To date, the most promising detector technology for IR detection in the mid to far IR band appears to be the HgCdTe eAPD (Mercury Cadmium Telluride electron Avalanche Photodiode). This technology has made significant advances in the past several years. These devices in general seem to provide the best overall speed and sensitivity (D*) over all known commercially available detector materials and configurations. However, with the present state-of-the-art, the advantage is significantly less at wavelengths beyond about 8 microns. Thus, at least in the near term, it would be advantageous to consider operation at these Mid IR wavelengths. It should be noted, however, that we also have developed an approved SBIR topic for the investigation and demonstration of advanced LWIR detector technologies, to be released in FY15.

An analysis of some of these intermediate wavelengths using the Kruse model also indicates that the greater part of the propagation gain (reduced scattering through atmospheric aerosols) demonstrated at 10 microns can be achieved with wavelengths in the Mid IR band, as shown in figure 22. QCL laser technology is also readily available at these wavelengths, making the construction of a deployable system a reasonable near-term goal. The addition of long range propagation testing of selected Mid IR wavelengths over the Griffiss-Stockbridge test bed is tentatively planned for FY15 or FY16.


Visibility	LWIR 10600 μ Prec/Ptx: dB	MWIR 4300 μ Prec/Ptx: dB	SWIR 1550 μ Prec/Ptx: dB
2	-91.373	-141.295	-248.5696
3	-55.4134	-83.2617	-153.3783
4	-41.8065	-58.6296	-108.335
5	-35.8213	-46.3745	-83.03901
6	-32.9623	-39.7182	-67.39639
7	-31.524	-35.8973	-57.11008
8	-30.7745	-33.6196	-50.05289
9	-30.3737	-32.2241	-45.05917
10	-30.1552	-31.3512	-41.44179
10.5	-30.086	-31.043	-40.00883
11	-30.0344	-30.7964	-38.77294
11.2	-30.0175	-30.712	-38.32668
11.7	-29.9831	-30.5306	-37.31626
12	-29.9667	-30.4392	-36.77478
12.2	-29.9572	-30.3845	-36.43803
12.5	-29.9448	-30.3107	-35.96634
13	-29.9284	-30.2067	-35.26066
14	-29.9065	-30.0541	-34.10182
15	-29.894	-29.9532	-33.20738
15.2	-29.8922	-29.9375	-33.05413
15.5	-29.8898	-29.9163	-32.83815
16	-29.8867	-29.8861	-32.51204
18	-29.88	-29.8109	-31.54028
20	-29.8778	-29.7767	-30.93391
22	-29.877	-29.7609	-30.5494
25	-29.8766	-29.7514	-30.21372
30	-29.8765	-29.7476	-29.96783
40	-29.8765	-29.7468	-29.84733

Figure 22. Multiple Band Plot

References

1. Maha Achour, PhD, UlmTech, Inc. Solana Beach, CA,   Free-Space Optics Wavelength Selection: 10µ Versus Shorter Wavelengths

2. K. S. Shaik, Atmospheric Propagation Effects Relevant to Optical Communications, TDA Progress Report 42-94. Jet Propulsion Laboratory, Pasadena, CA, April 22, 1988.

3. Andrew Hood, Allan Evans, and Manijeh Razeghi, Type-II Superlattices and Quantum Cascade Lasers for MWIR and LWIR Free-Space Communications, Proc. Of SPIE Vol 6900 (2008).

4. Free-Space Optics Propagation and Communication, Olivier Bouchet, Herve Sizun, Christian Boisrobert, Frederique de Fornel, Pierre-Noel Favennec, ISTE USA, Newport Beach, CA.

5. Optical Communications, Robert Gagliardi, Sherman Karp, John Wiley & Sons, Inc, 1995.

6. Free-Space Laser Communications, Arun Majumdar, Jennifer Ricklin, Springer 2008.

7. Mercury Cadmium Telluride Growth Properties and Applications, Peter Capper and James Garland, Wiley 2011.

8. Laser Communications in Space, Stephen Lambert and William Casey, Artech House 1995.

4   Toward an Integrated RF/FSO Link

(Mr. John Malowicki and Mr. David Hummel)

4.1   Introduction

A communication link for the purposes of system evaluation and experimental testing has been established by AFRL/RI between its Rome Research Site (RRS) and Stockbridge Test Site (STS). It includes an optical link based on an infrared (1550 nm) laser carrier, and an VW RF link in the 71-76 and 81-86 GHz bands. In the near future a Long wave IR capability will be added; see Section 3. This multi-band capability will serve to collect long term link performance data in all weather conditions. The analysis of this data will provide a better understanding of link availability and throughput which will help to set realistic expectations of the performance of future fielded systems.

4.2   System Overview

The RRS node is mounted on an 80' tower, immediately Southeast of Building 3 (N 43.22066˚, W 75.40755˚), at an altitude of approximately 550 ft above sea level. The Stockbridge node is temporarily mounted on scaffolding (N 43.02933˚, W 75.64585˚). By the end of 2014 a 70' tower will be installed at this location and the units will be mounted on the tower. Operating altitude is approximately 1350 - 1380 ft above sea level.   Figure 23 shows the two locations and line of site in a map view. Figures 24 and 25 show aerial views of the RRS and Stockbridge sites, respectively. The ground elevation profile is shown in figure 26. Accounting for tower heights, the elevation angle from the RRS node to the STS node (at the highest tower position) is 0.56 degrees.
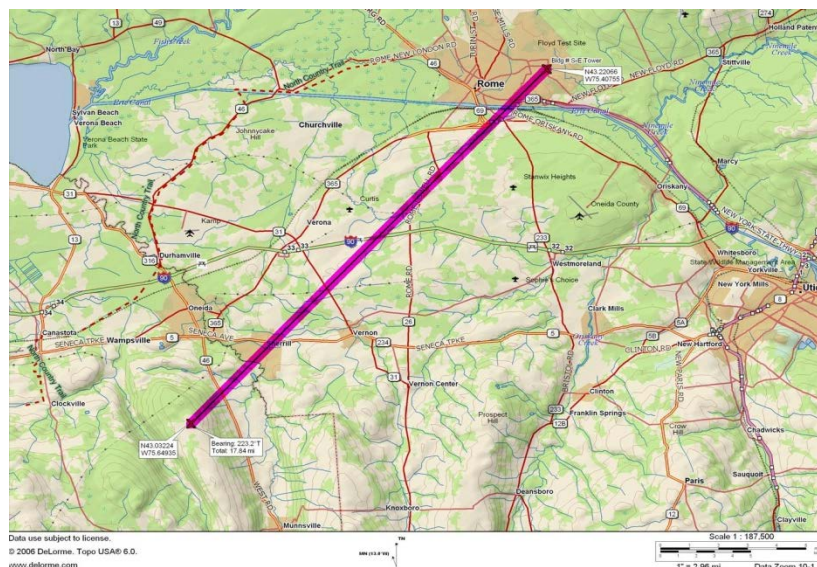

Figure 23. Map of Line of Sight Optical Path

To Stockbridge
Bearing 232.2°

Figure 24. Rome Site

To RRS
Bearing 52.2°
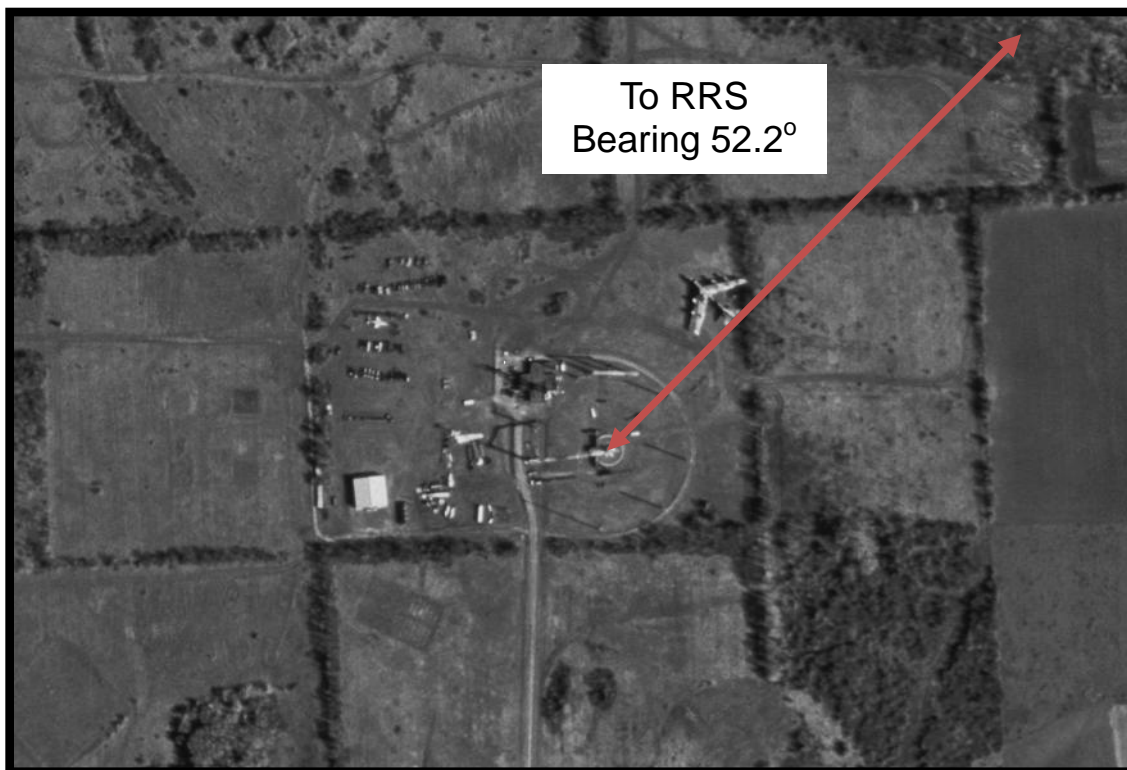
Figure 25. Stockbridge Site
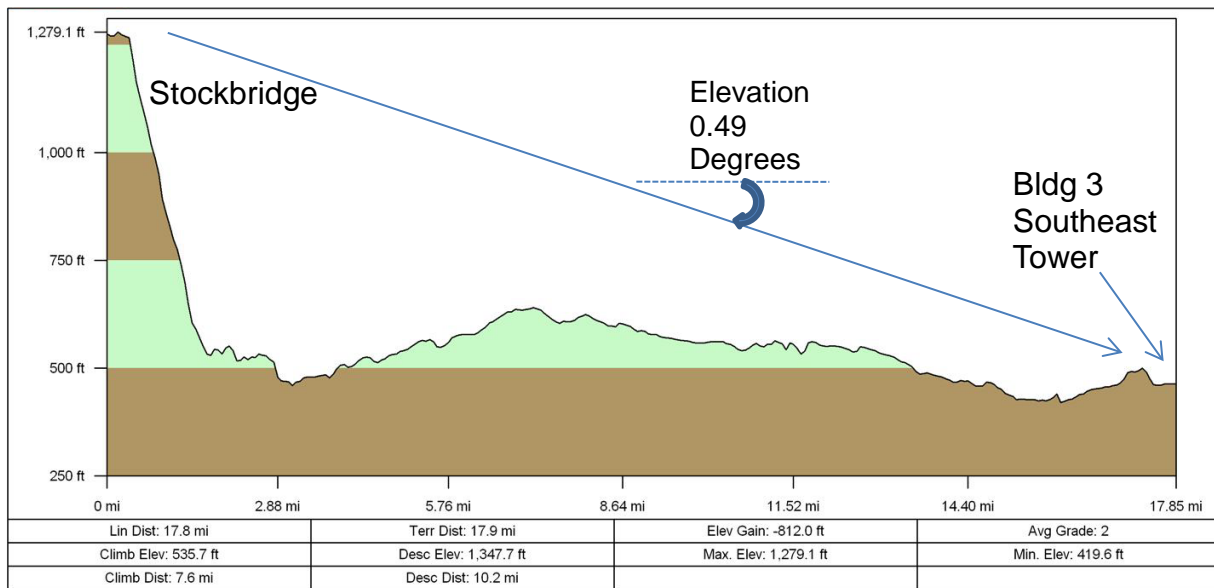
Figure 26. Elevation Profile

4.3 Parameters of the Optical System

The optical terminal is manufactured by AOptix and is similar to the units developed under the DARPA FOENEX program.

- Beacon Laser Diode Array
    - Wavelength: 850 nm
    - Optical power: 10 mW (reduced to 1 mW with ND filter)
    - Beam Divergence: 0.2 deg full angle
    - Path distance: 28 km
    - Beam size at receiver: ~100 m diameter
- Communications Laser
    - Wavelength: 1545.31 and 1555.74 nm
    - Optical power: Maximum 1.5 W output (but restricted to 1 W for increased safety)
    - Transmit Optical Aperture: 10 cm diameter, circular
    - Beam Divergence: ~16 µrad (diffraction-limited)
    - Path distance: 28 km
    - Beam size at receiver: ~45 cm diameter

4.4 Parameters of the RF System

The VW system is commercially available from BridgeWave Communications and is a model AR80 with 24" dish.

- Frequency: $71 - 76$ GHz and $81 - 86$ GHz
- Link Budget:
    - Gigabit Ethernet Mode: 186 dB @ 10^{-12} B.E.R.
- Antenna Parameters
    - Size: 24" (60 cm) Parabolic
    - Main Lobe Beam width: 0.4 degrees
    - Peak Gain: 23 dB

4.5   Link Budget – Optical System

A first approximation link budget can be calculated in eq. 4.1 using simple geometrical and atmospheric attenuation assumptions. Figure 27 illustrates the geometry of the transmitted beam and the collecting aperture at the receiver. Using the diameter of the transmit optics and assuming a divergence *D*, a ratio of the area of the collection optics to the beam size at the receiver can be calculated. This ratio multiplied by the power transmitted and a loss factor for atmospheric attenuation represented by α, gives an estimate of the received optical power. The value of the atmospheric attenuation can be estimated from Table 1 based on the optical visibility of the atmospheric path.

$$P_{received} = P_{transmitted} * \frac{d_2^2}{\left(d_1 + \left(D*R\right)\right)^2} * 10^{\left(-\alpha*R/10\right)}$$

(4.1)
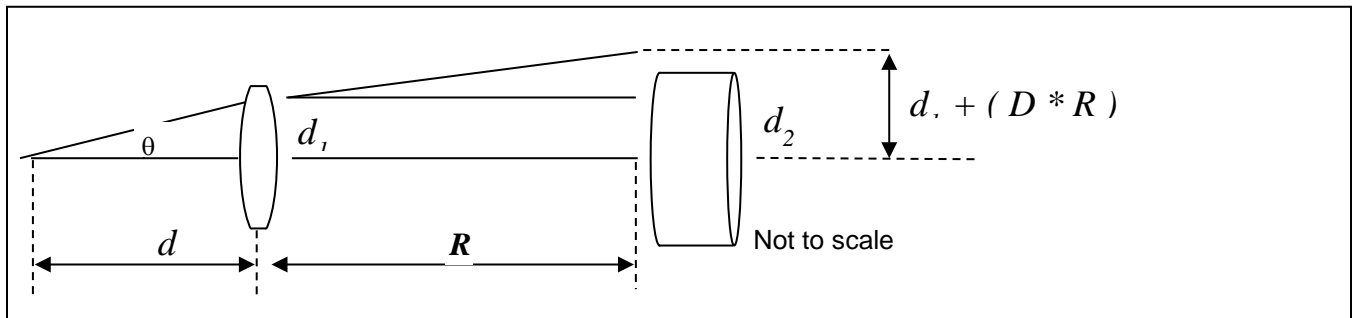

Figure 27. Link Budget between Stockbridge and Rome

Table 8

Weather Condition	Precipitation		Amount mm/hr	Visibility	dB Loss/km
Dense fog				0 m, 50 m	–271.65
Thick fog				200 m	–59.57
Moderate fog	snow			500 m	–20.99
Light Fog	snow	Cloudburst	100	770 m	–12.65
				1 km	–9.26
Thin fog	snow	Heavy rain	25	1.9 km	–4.22
				2 km	–3.96
Haze	snow	Medium rain	12.5	2.8 km	–2.58
				4 km	–1.62
Light haze	snow	Light rain	2.5	5.9 km	–0.96
				10 km	–0.44
Clear	snow	Drizzle	0.25	18.1 km	–0.24
				20 km	–0.22
Very Clear				23 km	–0.19
				50 km	–0.06

Figure 28. Optical terminal and VW antenna at Rome
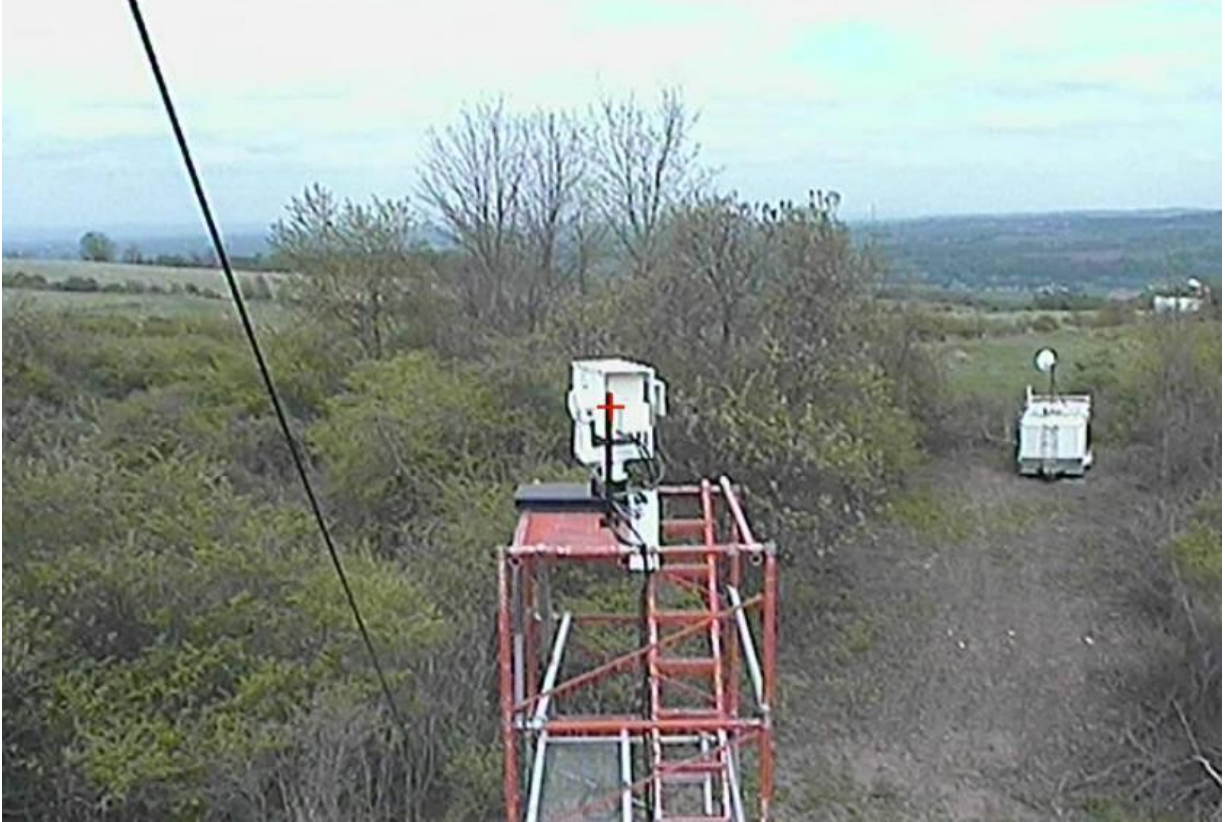
Figure 29. Optical terminal and Rapidlink antenna at Stockbridge

4.6   Upgrade – Optical System

An upgrade to the optical system was initiated with an aim towards better pointing and tracking performance and increased communication bandwidth. Improvement to the pointing and tracking was needed since often times the link would be broken by external factors like strong winds and there was no automatic mechanism to re-establish the link. Manual intervention was required to close the link again. This made collection of long term link performance statistics nearly impossible. A new control system with a better gimbal promised a more robust pointing and tracking system which would enable better data collection and make the link usable for quantum communication type experiments.

The improvements were in two main areas: a better gimbal from Cobham Sensor Systems, shown below in figure 29, and incorporation of its coarse pointing functionality into the system control loop. The AOptix terminal takes the place of the mounting plates shown in figure 29, and sits between the gimbal forks. The general idea is that the deformable mirror would handle the correction for small changes in the angle of arrival of the signal beam, along with the higher order corrections, but when the pointing moved beyond the range of the mirror, the control system would tell the gimbal to make a gross correction to the pointing. Details of the upgrade follow. In the fall of 2013 AOptix delivered an upgraded optical system.
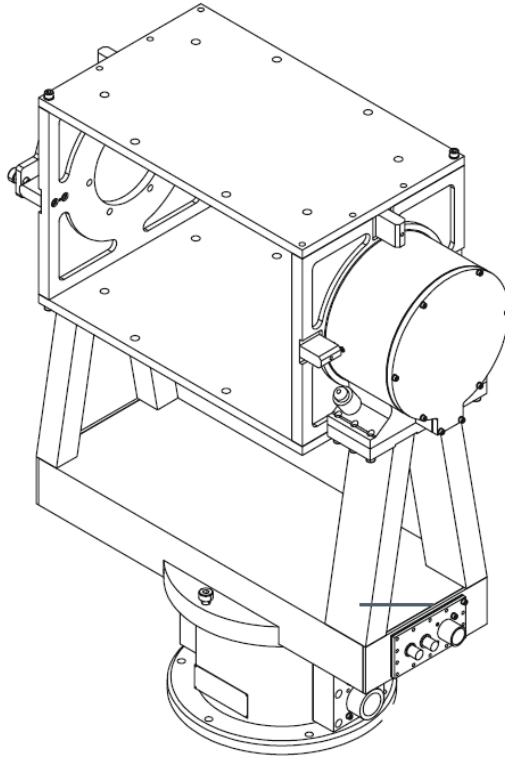
Figure 30. SPS-500 Positioner

Laser Terminals Upgrade:

1) Control circuit electronics and software upgrade to the AOptix laser comm. terminals to improve link lock and performance.

Specifically:

PCBA: PC Board Assembly
AOC: Adaptive Optics Control
HVA: High Voltage Amp
WFS: Wavefront Sensor
MM: Membrane Mirror
NFOV: Narrow Field of View

Upgrade of the PCBAs (AOC, HVA, WFS, MM electronics). The re-designed AOC PCBA with DSP1 and DSP2 upgrades from 600 MHz to 1 GHz, improved system closed-loop bandwidth up to 50 percent (from 1.0Khz to 1.5Khz). The re-designed MM PCBA facilitates monitoring of environmental conditions of membrane mirror (MM). Additionally, the new circuit design supports DWDM reference sources at 1545 and 1555nm with power targets of 0 to 20dBm. The re-designed WFS PCBA circuit improves bandwidth matching, noise gain peaking, increased dynamic range and improved sensitivity. This also includes upgraded software for the system that allows interaction with the new board set, among other improvements.
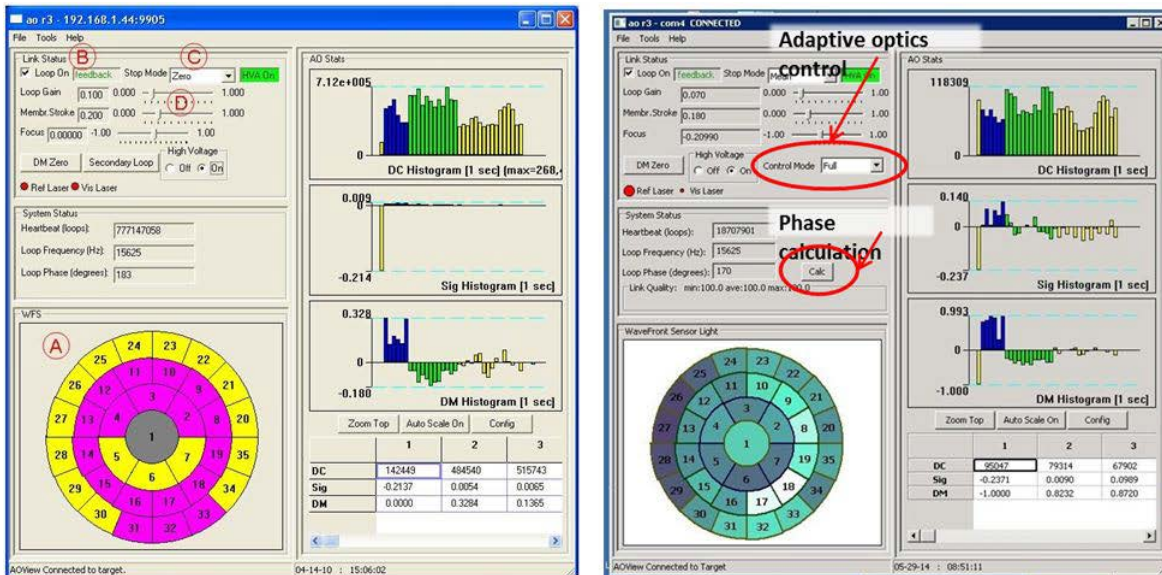
Figure 31.   Previous AOptix control   Updated AOptix control interface

2) Gimbal: The previous FLIR (or formerly Directed Perception) PTU-D300 gimbals were not designed for continuous pointing in the control loop. They are for rough pointing only. Additionally, the PTU-D300 had a pointing resolution of 0.006429°, which the Cobham Sensor Systems SPS-500 Positioner and Control System improved upon with ± 0.002° accuracy. Complete SPS-500 gimbal specs are in Table 9.

Table 9. SPS Gimbal Specifications.

Description	Value
Positioner	
Dimensions (without payload)	23.41 H x 18.23 W x 8.0 D inches
Weight, positioner/riser	35.2 lb
Weight, payload	35 lb (estimated); 70 lb (maximum)
Weight, total	105.2 lb (maximum)
Azimuth torque	10 ± 1 ft lbs.
Elevation torque	5 ± 1 ft. lbs.
Azimuth travel	± 180°
Elevation travel	-10° to +80° ± 1°
Mechanical stops	Azimuth: ± 275°; elevation: − 35° and + 215°
Azimuth speed; acceleration	180°/sec; 180°/sec^2
Elevation speed; acceleration	180°/sec; 180°/sec^2
Repeatability, az and el	± 0.002°

The software interface differences are highlighted in figure 31, showing the before and after user interface, respectively. The new software allows user control of the adaptive optics implementation. Now the user can choose between full, higher order correction or tip-tilt only correction. This can be useful in demonstrating the improved signal performance with the higher order correction. Additionally, the method for setting the best loop phase for the feedback control has been automated with a simple single click button which calculates the phase number and sets it. In figure 31 items A- D highlight the main control features and are described as follows: A – a representation of the 32 segments of the wavefront sensor which is color coded by the number of detection counts, this also corresponds to the deformable mirror segmentation; B – the toggle control for turning the control loop on or off; C – the mode for setting the mirror rest state; D – the slider bars to adjust the control loop feedback parameters.

4.7   Results – Optical Link

The optical link was finally re-established from Rome to Stockbridge in May of 2014. The performance was similar to that of the initial system in terms of actual link performance. The pointing and tracking control system has not been fully tested due to many systems integration issues as well as external test site issues. An example of the measured link data is shown in figure 32 below. The drop out of the signal at about 7:40 is due to user adjustments. This can be compared to the previous link performance over 3 days' time from May 2011 as shown in figure 33.
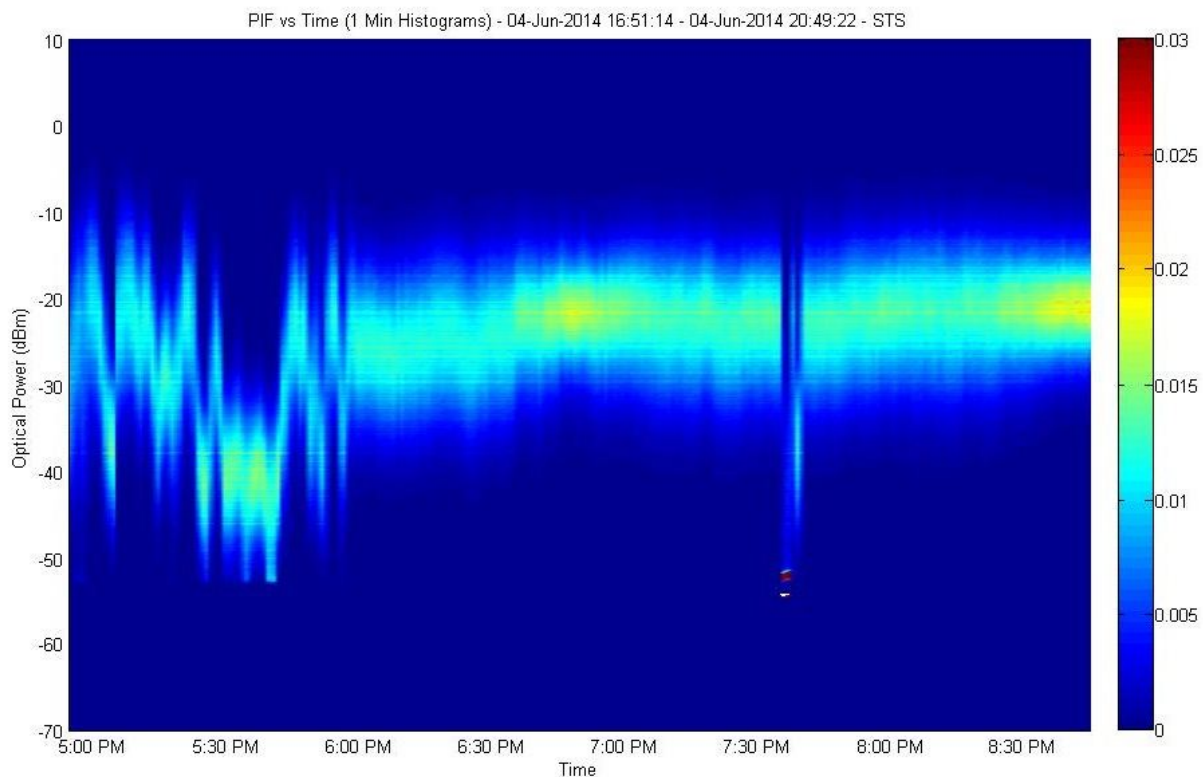

Figure 32– Link performance on June 4th 2014
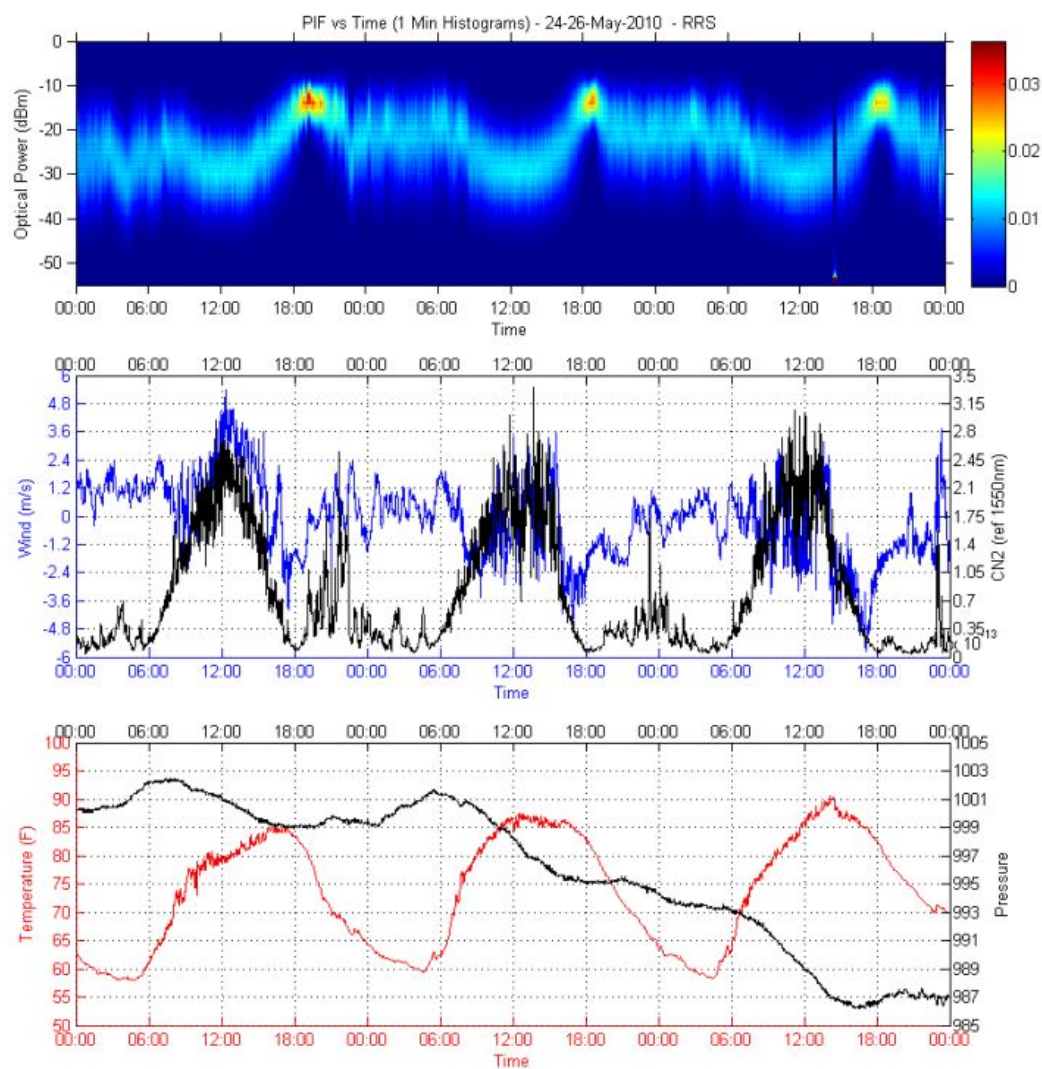
Figure 33. Link performance over 24-26 May 2010

5   Photon Entanglement Transport Through a Hyperspectral Filter

(Dr. David H. Hughes and Dr. Reinhard Erdmann)

5.1   Introduction

Our in-house work asked the question, can a multi-access hyperspectral telescope maintain entanglement between spontaneously generated photon pairs in four wave mixing processes, thus providing shared secret key material to seed stream ciphers for data encryption? If not, can the telescope be modified to do so, or should another quantum key distribution protocol be implemented that does not rely on entanglement?

Funded by AFOSR, our current investigations are motivated in a contractual effort funded by AFRL 6.2 to integrate two technologies, a keyed quantum communication secret key distribution system, and a multi-access laser communications system. The former technology utilizes entangled photon pairs to distribute secret keys and is highly quantum mechanical. The latter technology utilizes a Lyot filter based hyperspectral tree for wavelength division multiplexing, in both transmit and receive, for high data rate classical optical communications. It is designed for communications between a hub and several spokes.

5.2   Background

The two technologies to be integrated in the 6.2 contractual effort are shown in figure 34. NuCrypt LLC developed the entangled pair source and detection systems with supporting funding by an AFRL/AFOSR STTR [1], while Optical Physics Company developed the multi-access hyperspectral telescope under an AFRL/SMC SBIR [2].

Multi-Access Lasercom   Entangled Pair Generation and Detection
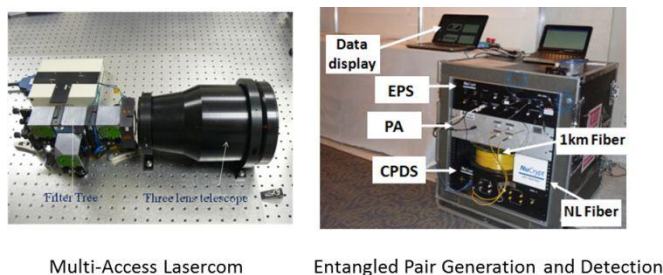
Figure 34. A multi-access hyperspectral telescope (left) is to be integrated with an entangled photon source and receiver (right).

The hyperspectral filter configuration on the left of figure 34 supports four simultaneous users. It will be modified to construct three telescopes, each supporting two simultaneous users. A core functional element of the hyperspectral telescope is the filter tree comprised of Lyot stages [3]. Each Lyot stage comprises a Lyot filter stack followed by a polarizing beam splitter (PBS) made of silicon. This is shown in figure 35. Incident frequencies chosen from the ITU grid, separated by approximately 200 GHz, are either congruent or incongruent with respect to the birefringence of each Lyot stack. Basically, the Lyot stack will leave invariant the polarization state of a congruent frequency, but rotate an incongruent frequency polarization by $\pi/2$. The polarization beam splitter, rotated by $\pi/4$ with respect to the Lyot stack optical axis, projects horizontal and vertical inputs with respect to its splitter interface into orthogonal directions. This is accomplished by total internal reflection by S polarized states, here the horizontal states, and frustrated internal reflection, or transmission, by P polarized states, here the

vertical states. S polarized states possess polarization states orthogonal to the plane of incidence. P polarized states possess polarization states parallel to that plane; they tunnel across an air gap at the interface between the two silicon prisms comprising the PBS. For proper operation, all frequencies are chosen from the ITU 200 GHz grid. We denote the congruent frequency f_1, and incongruent frequency f_2.
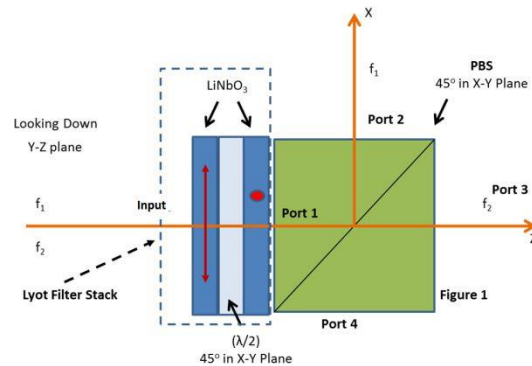

Figure 35 Lyot filter stage comprised of a Lyot filter stack followed by a polarizing beam splitter, or PBS. Here, f_1 is congruent and f_2 incongruent with the Lyot stack. Both are incident at $\pi/4$ on the Lyot stack, but f_2 was rotated by $\pi/2$ and is parallel to the plane of incidence of the PBS.
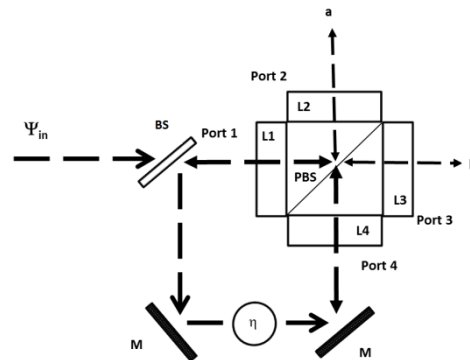

Figure 36. Entangled photon pair amplitudes enter one port of a beam splitter (BS). There they split into two paths. They recombine when entering a modified Lyot filter stage at Port 1 and Port 2; classically, we would say Port 1 *or* Port 2.

In principal, NuCrypt LLC's entangled photon pair source can emit entangled pairs collinearly such that those pairs arrive along a line at the Lyot filter stack. That will not be implemented in the 6.2 integration project. In order to have a ghost of a chance at accomplishing a quantum key distribution protocol, classical communications are necessary. Leakage between the classical channels, though not fatal to the classical communications, would swamp the quantum channel. Instead, in the 6.2 contractual effort the quantum and classical channels are split right away and processed separately.

Our 6.1 basic research thrust here, funded by AFOSR LRIR13RI08COR, focuses on modeling photon entanglement transport through a modified Lyot hyperspectral stage in the absence of classical signals. Shown in figure 36 is the modified hyperspectral stage. Lyot stacks L1 and L4 are identical. They effect differential changes in the polarization states of f_1 and f_2 photons. Lyot stacks L2 and L3 are identical as well, but effect no polarization changes in either input frequency. Future research and reporting will vary these parameters. For now, we will first concentrate on just L1 to understand the behavior of the

entangled state transiting it, then add L4 and a beam splitter to present the possibility that the input entangled state enters the PBS from P_1 or P_4.

5.3 Entanglement Transport

Consider an entangled photon pair input into the P_1 port of the Lyot filter stage wherein one frequency is congruent with the Lyot stack and the other is incongruent. Label them f_1 and f_2 respectively. They are generated in a spontaneous four wave mixing process wherein energy and photon spin are conserved. A quantum joint state generated by the process can be written in terms of the Lyot stack reference frame or the polarization beam splitter frame (PBS) as below:

$$\left| a_{in} \right\rangle = \frac{1}{\sqrt{2}} \left(\begin{array}{c} \dfrac{\left(\left| f_1, h, P_1 \right\rangle_1 + \left| f_1, v, P_1 \right\rangle_1 \right)}{\sqrt{2}} \otimes \dfrac{\left(\left| f_2, h, P_1 \right\rangle_2 + \left| f_2, v, P_1 \right\rangle_2 \right)}{\sqrt{2}} \\[4mm] + \dfrac{\left(\left| f_1, h, P_1 \right\rangle_1 - \left| f_1, v, P_1 \right\rangle_1 \right)}{\sqrt{2}} \otimes \dfrac{\left(\left| f_2, h, P_1 \right\rangle_2 - \left| f_2, v, P_1 \right\rangle_2 \right)}{\sqrt{2}} \end{array} \right)$$

$$(5.1a)$$

$$= \tfrac{1}{\sqrt{2}} \left(\left| f_1, H, P_1 \right\rangle_1 \left| f_2, H, P_1 \right\rangle_2 + \left| f_1, V, P_1 \right\rangle_1 \left| f_2, V, P_1 \right\rangle_2 \right)$$

Symbols f_1 and f_2 refer to the input frequencies. H and V refer to horizontal and vertical polarizations in the PBS reference frame, while symbols h and v refer to horizontal and vertical polarization with respect to the Lyot stack, oriented at $\pi/4$ with respect to the PBS in figure 35. P_1 is the leftmost port where a state first enters the Lyot stage, as shown in figure 35. Commas between the elements within a ket are shorthand for tensor product symbols, product signs ensconced within circles. A comma is used to save space on the page within an equation. Subscripts on the kets refer to the fact that there are two photons emitted in the four wave mixing process, each having degrees of freedom listed within the ket. That is, each photon has probability amplitudes associated to them. Which set of photon amplitudes to label '1' and '2' is our choice. That two photons are emitted by a physical process under conditions we engineer a possibility to achieve, estimated by us with probabilities of occurrence, is not up to us. It is decided by nature. A mathematical way to express this is to say that each photon state resides in their respective Hilbert spaces. Those Hilbert spaces are entangled or they are not.

We will often write (5.1a) in the more condensed notation of (5.1b),

$$\left| a_{in} \right\rangle = \tfrac{1}{\sqrt{2}} \left(\left| f_1, H, P_1; f_2, H, P_1 \right\rangle + \left| f_1, V, P_1; f_2, V, P_1 \right\rangle \right) \tag{5.1b}$$

Semicolons divide the two Hilbert spaces. Because we have two Hilbert spaces comprising the joint state, the subscripts on the kets sometimes remain. Position wise, however, subspace 1 is the left ket subspace 2 is the right ket. If we label the frequencies μ and ν those subscripts or the position of the kets will remain 1 and 2. In this system, frequency is immutable. It really defines the existence of each Hilbert subspace in the joint distribution. In essence, it is not so hidden a variable.

The Lyot stack is represented by a series of unitary operations [6],

$$
\begin{array}{ccc}
\boxed{\begin{array}{c}\text{(3) LiNbO}_3\text{ Plate}\\[4pt]
\begin{bmatrix} 0 & -1 \\ 1 & 0 \end{bmatrix}\begin{bmatrix} e^{-i\frac{\phi_j}{2}} & 0 \\ 0 & e^{i\frac{\phi_j}{2}} \end{bmatrix}\begin{bmatrix} 0 & 1 \\ -1 & 0 \end{bmatrix}=\begin{bmatrix} e^{i\frac{\phi_j}{2}} & 0 \\ 0 & e^{-i\frac{\phi_j}{2}} \end{bmatrix}\end{array}}
&
\boxed{\begin{array}{c}\text{(2) Half Wave Plate}\\[4pt]
\begin{bmatrix} \frac{1}{\sqrt2} & \frac{-1}{\sqrt2} \\ \frac{1}{\sqrt2} & \frac{1}{\sqrt2} \end{bmatrix}\begin{bmatrix} -i & 0 \\ 0 & i \end{bmatrix}\begin{bmatrix} \frac{1}{\sqrt2} & \frac{1}{\sqrt2} \\ \frac{-1}{\sqrt2} & \frac{1}{\sqrt2} \end{bmatrix}=\begin{bmatrix} 0 & -i \\ -i & 0 \end{bmatrix}\end{array}}
&
\boxed{\begin{array}{c}\text{(1) LiNbO}_3\text{ Plate}\\[4pt]
\begin{bmatrix} e^{-i\frac{\phi_j}{2}} & 0 \\ 0 & e^{i\frac{\phi_j}{2}} \end{bmatrix}\end{array}}
\end{array}
\tag{5.2}
$$

In the Lyot stack frame, the Lyot filter is the product of the unitary operators in equation 5.2, given by,

$$
\begin{bmatrix} e^{i\frac{\phi_j}{2}} & 0 \\ 0 & e^{-i\frac{\phi_j}{2}} \end{bmatrix}\begin{bmatrix} 0 & -i \\ -i & 0 \end{bmatrix}\begin{bmatrix} e^{-i\frac{\phi_j}{2}} & 0 \\ 0 & e^{i\frac{\phi_j}{2}} \end{bmatrix}=\begin{bmatrix} 0 & -ie^{i\varphi_j} \\ -ie^{-i\varphi_j} & 0 \end{bmatrix}.
\tag{5.3}
$$

Index 'j' takes values {1,2}, and refers to frequencies f_1 and f_2 . ϕ_j is the optical path length difference (OPD) phase for each plate and φ_j is the cumulative OPD phase for the stack. Congruent frequencies possess cumulative OPD phases $\varphi_j = \pi$, for a total OPD phase of 2π, while incongruent frequencies possess cumulative OPD phases $\varphi_j = \pi/2$, for a total OPD phase of π. Thus the actions of the Lyot stack on congruent and incongruent frequency states is a function of the input frequency,

$$
L_{f1}=\begin{bmatrix} 0 & -ie^{i\pi} \\ -ie^{-i\pi} & 0 \end{bmatrix}=\begin{bmatrix} 0 & i \\ i & 0 \end{bmatrix}=i\sigma_1 \qquad L_{f2}=\begin{bmatrix} 0 & -ie^{i\frac{\pi}{2}} \\ -ie^{-i\frac{\pi}{2}} & 0 \end{bmatrix}=\begin{bmatrix} 0 & 1 \\ -1 & 0 \end{bmatrix}=i\sigma_2 ,
\tag{5.4}
$$

where

$$
\sigma_1=\begin{bmatrix} 0 & 1 \\ 1 & 0 \end{bmatrix},\sigma_2=\begin{bmatrix} 0 & -i \\ i & 0 \end{bmatrix},\sigma_3=\begin{bmatrix} 1 & 0 \\ 0 & -1 \end{bmatrix}, \text{ and } \sigma_0=\begin{bmatrix} 1 & 0 \\ 0 & 1 \end{bmatrix}.
\tag{5.5}
$$

It is important to remind oneself that the Lyot filter stack as constructed is a device employing birefringence to operate on input states whose frequencies are either congruent or incongruent with the thickness of the birefringent plates comprising the filter stack. This allows one to vary the input frequencies, or vary the birefringence of the Lyot filters in an active manner to gain different outputs, a capability about which more will be reported after further investigation.

States expressed in the computational basis are:

$$
|h\rangle \rightarrow \begin{bmatrix} 1 \\ 0 \end{bmatrix} \qquad |v\rangle \rightarrow \begin{bmatrix} 0 \\ 1 \end{bmatrix}
\tag{5.6}
$$

So that,

$$
|a_h\rangle = \begin{bmatrix} |h\rangle & |v\rangle \end{bmatrix}\begin{bmatrix} \frac{1}{\sqrt2} \\ \frac{1}{\sqrt2} \end{bmatrix} = \tfrac{1}{\sqrt2}(|h\rangle+|v\rangle) \quad \text{and} \quad |a_v\rangle = \begin{bmatrix} |h\rangle & |v\rangle \end{bmatrix}\begin{bmatrix} \frac{1}{\sqrt2} \\ \frac{-1}{\sqrt2} \end{bmatrix} = \tfrac{1}{\sqrt2}(|h\rangle-|v\rangle)
\tag{5.7}
$$

For the fixed Lyot filter stacks of equation (5.4), their action on the congruent and incongruent input states of equation (5.1) are, suppressing the port index for now,

$$L_{f1}|a_{h1}\rangle = \begin{bmatrix} |h\rangle_1 & |v\rangle_1 \end{bmatrix} i\sigma_1 \begin{bmatrix} \frac{1}{\sqrt{2}} \\ \frac{1}{\sqrt{2}} \end{bmatrix} = \begin{bmatrix} |h\rangle_1 & |v\rangle_1 \end{bmatrix} \begin{bmatrix} 0 & i \\ i & 0 \end{bmatrix} \begin{bmatrix} \frac{1}{\sqrt{2}} \\ \frac{1}{\sqrt{2}} \end{bmatrix} = \frac{i}{\sqrt{2}}\left(|h\rangle_1 + |v\rangle_1\right)$$

$$L_{f1}|a_{v1}\rangle = \begin{bmatrix} |h\rangle_1 & |v\rangle_1 \end{bmatrix} i\sigma_1 \begin{bmatrix} \frac{1}{\sqrt{2}} \\ \frac{-1}{\sqrt{2}} \end{bmatrix} = \begin{bmatrix} |h\rangle_1 & |v\rangle_1 \end{bmatrix} \begin{bmatrix} 0 & i \\ i & 0 \end{bmatrix} \begin{bmatrix} \frac{1}{\sqrt{2}} \\ \frac{-1}{\sqrt{2}} \end{bmatrix} = \frac{-i}{\sqrt{2}}\left(|h\rangle_1 - |v\rangle_1\right)$$

(5.8a-5.8d)

$$L_{f2}|a_{h2}\rangle = \begin{bmatrix} |h\rangle_2 & |v\rangle_2 \end{bmatrix} i\sigma_2 \begin{bmatrix} \frac{1}{\sqrt{2}} \\ \frac{1}{\sqrt{2}} \end{bmatrix} = \begin{bmatrix} |h\rangle_2 & |v\rangle_2 \end{bmatrix} \begin{bmatrix} 0 & 1 \\ -1 & 0 \end{bmatrix} \begin{bmatrix} \frac{1}{\sqrt{2}} \\ \frac{1}{\sqrt{2}} \end{bmatrix} = \frac{1}{\sqrt{2}}\left(|h\rangle_2 - |v\rangle_2\right)$$

$$L_{f2}|a_{v2}\rangle = \begin{bmatrix} |h\rangle_2 & |v\rangle_2 \end{bmatrix} i\sigma_2 \begin{bmatrix} \frac{1}{\sqrt{2}} \\ \frac{-1}{\sqrt{2}} \end{bmatrix} = \begin{bmatrix} |h\rangle_2 & |v\rangle_2 \end{bmatrix} \begin{bmatrix} 0 & 1 \\ -1 & 0 \end{bmatrix} \begin{bmatrix} \frac{1}{\sqrt{2}} \\ \frac{-1}{\sqrt{2}} \end{bmatrix} = \frac{-1}{\sqrt{2}}\left(|h\rangle_2 + |v\rangle_2\right)$$

But for a phase, the Lyot stack leaves invariant polarizations of congruent frequency states, while rotating polarizations of incongruent frequency states by $\pi/2$. The two frequencies live in distinct Hilbert spaces, which are subspaces of the joint state. That fact implies unitary operations on states in one subspace do not effect changes in states in the other subspace. Both states propagate collinearly through the Lyot stack, for now assumed a perfect, lossless device.

Polarization entanglement in the joint state is preserved in transit through the Lyot stack. Prior to entering the stack, the joint state given in equation (5.1) can be written as a combination of two Hilbert subspaces via a Jordan-Schwinger representation [7, 8]. See Appendix 5.A.

$$|a_{in}\rangle = \begin{bmatrix} |h\rangle_1 & |v\rangle_1 \end{bmatrix} \left(U_1 R U_2^{\dagger}\right) \begin{bmatrix} |h\rangle_2 \\ |v\rangle_2 \end{bmatrix}$$

$$= \begin{bmatrix} \frac{(|h\rangle_1 + |v\rangle_1)}{\sqrt{2}} & \frac{(|h\rangle_1 - |v\rangle_1)}{\sqrt{2}} \end{bmatrix} \frac{\sigma_0}{\sqrt{2}} \begin{bmatrix} \frac{(|h\rangle_2 + |v\rangle_2)}{\sqrt{2}} \\ \frac{(|h\rangle_2 - |v\rangle_2)}{\sqrt{2}} \end{bmatrix}$$

(5.9)

$$= \frac{1}{\sqrt{2}}\left(\left(\frac{(|h\rangle_1 + |v\rangle_1)}{\sqrt{2}}\frac{(|h\rangle_2 + |v\rangle_2)}{\sqrt{2}}\right) + \left(\frac{(|h\rangle_1 - |v\rangle_1)}{\sqrt{2}}\frac{(|h\rangle_2 - |v\rangle_2)}{\sqrt{2}}\right)\right)$$

Or, inserting the port subscript and expressing in the PBS basis, (5.1) is recovered.

$$|a_{in}\rangle = \frac{1}{\sqrt{2}}\left(|f_1,H,P_1\rangle_1 |f_2,H,P_1\rangle_2 + |f_1,V,P_1\rangle_1 |f_2,V,P_1\rangle_2\right)$$

(5.10)

Under the action of the Lyot stack, however, and according to equations (4.8),

$$\left|a_{out}\right\rangle = \begin{bmatrix}\left|h\right\rangle_1 & \left|v\right\rangle_1\end{bmatrix}\left(L_1 U_1 R\, U_2^\dagger L_2^\dagger\right)\begin{bmatrix}\left|h\right\rangle_2 \\ \left|v\right\rangle_2\end{bmatrix}$$

$$= \begin{bmatrix}\left|h\right\rangle_1 & \left|v\right\rangle_1\end{bmatrix}\left(i\sigma_1\frac{(\sigma_1+\sigma_3)}{\sqrt{2}}\right)\frac{\sigma_0}{\sqrt{2}}\left(\frac{(\sigma_1+\sigma_3)}{\sqrt{2}}(-i\sigma_2)\right)\begin{bmatrix}\left|h\right\rangle_2 \\ \left|v\right\rangle_2\end{bmatrix} \qquad (5.11)$$

$$= \begin{bmatrix}\left|h\right\rangle_1 & \left|v\right\rangle_1\end{bmatrix}\begin{bmatrix}0 & i \\ i & 0\end{bmatrix}\begin{bmatrix}\frac{1}{\sqrt{2}} & \frac{1}{\sqrt{2}} \\ \frac{1}{\sqrt{2}} & \frac{-1}{\sqrt{2}}\end{bmatrix}\begin{bmatrix}\frac{1}{\sqrt{2}} & 0 \\ 0 & \frac{1}{\sqrt{2}}\end{bmatrix}\begin{bmatrix}\frac{1}{\sqrt{2}} & \frac{1}{\sqrt{2}} \\ \frac{1}{\sqrt{2}} & \frac{-1}{\sqrt{2}}\end{bmatrix}\begin{bmatrix}0 & -1 \\ 1 & 0\end{bmatrix}\begin{bmatrix}\left|h\right\rangle_2 \\ \left|v\right\rangle_2\end{bmatrix}$$

Or, inserting the port, P1, and using the condensed notation,

$$\left|a_{out}\right\rangle = \tfrac{i}{\sqrt{2}}\left(\left|f_1,H,P_1;f_2,V,P_1\right\rangle + \left|f_1,V,P_1;f_2,H,P_1\right\rangle\right) = \left|b_{in}\right\rangle$$

$$\left|a_{out}\right\rangle = \tfrac{i}{\sqrt{2}}\left(\left|f_1,h,P_1;f_2,h,P_1\right\rangle + \left|f_1,v,P_1;f_2,v,P_1\right\rangle\right) = \left|b_{in}\right\rangle \qquad (5.12)$$

Equations (5.12) express the exit state into P1 in figure 35 in terms of the PBS and Lyot reference frames respectively. The input state to the system, equation (5.1) is rotationally invariant. The output state from the Lyot stack, 'b_{in},' into the PBS, is not.

Symbol, R, in equations (5.9) is the operator connecting the two Hilbert subspaces. It doesn't always describe an entangled state. It can describe all four of the so-called maximally entangled Bell states if R is one of the normalized basis elements in equation (5.5). The Bell states span the four dimensional space of two-qubit composite systems. For example, a linear combination of them can describe mixed states that are not entangled. See Appendix 5.A.
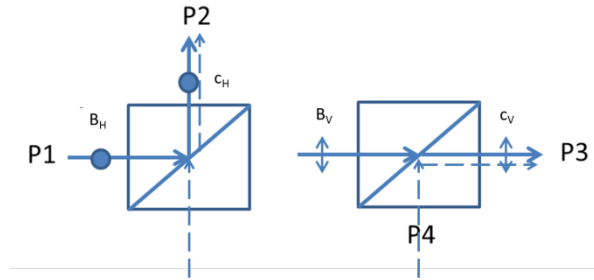
Figure 37 Action of the PBS on the input states. A vacuum state into the PBS is indicated by the dashed line. We fill that vacuum with the possibility that the entangled state enters at P4 as well as P1 by placing a BS in the input path as shown in Figure 36.

We now add the possibility of the state entering P4 as well as P1, as shown in figure 35. Two photons of an entangled pair enter the BS from the same port. They both exit the BS, entering P1 port of figure 36. The modified Lyot stage is comprised of four Lyot filter stacks followed by a polarizing beam splitter, or PBS. Here, f_1 is congruent and f_2 incongruent with the Lyot stacks, L1 and L4. However, in this model both are congruent with L2 and L3. M is a mirror, BS is a non-polarizing beam splitter, and η is a phase adjustment. It rectifies the phase due to path length difference and reflections between the two possible ways the entangled state enters the Lyot stage. After passing through the BS, the state input into the Lyot stage can be expressed as,

$$|a_{in}\rangle = \frac{1}{2}\left(\left|\Psi_0\left(H_1P_1;H_2P_1\mid V_1P_1;V_2P_1\right)\right\rangle + \left|\Psi_0\left(H_1P_4;H_2P_4\mid V_1P_4;V_2P_4\right)\right\rangle\right)$$
$$\frac{1}{2}\left(\left|\Psi_0\left(H_1P_1;H_2P_4\mid V_1P_1;V_2P_4\right)\right\rangle + \left|\Psi_0\left(H_1P_4;H_2P_1\mid V_1P_4;V_2P_1\right)\right\rangle\right)$$

(5.13)

The Ψ functions are called Bell state forms. They collect probability amplitudes possessing different degrees of freedom into convenient algebraic forms. See Appendix 5.A. Passing through the Lyot stack, and then the PBS, and expressing the resulting state in the PBS frame, we arrive at,

$$|c_{out}\rangle = \frac{1}{2}\left(\left|\Psi_0\left(H_1P_2;V_2P_3\mid V_1P_3;H_2P_2\right)\right\rangle + \left|\Psi_0\left(H_1P_3;V_2P_2\mid V_1P_2;H_2P_3\right)\right\rangle\right)$$
$$\frac{1}{2}\left(\left|\Psi_0\left(H_1P_2;V_2P_2\mid V_1P_3;H_2P_3\right)\right\rangle + \left|\Psi_0\left(H_1P_3;V_2P_3\mid V_1P_2;H_2P_2\right)\right\rangle\right)$$

(5.14)

Basically, the Lyot stack performs rotations on the input state, setting it up for path projection by the PBS. PBS is a polarization projector. But it is also a unitary operator [8,9]. (5.14) contains eight states over sixteen single constituent bases. Those states are distributed according to the Bell state form in which they are contained. Inspect closely, however, the degrees of freedom in both (5.13) and (5.14.) As sets, they are all different. For that reason every one of the above forms is orthogonal to all the others. Since each Bell form is normalized by the square root of two, they form an orthonormal basis.

Since the BS breaks the symmetry of one dimensional collinear propagation, new modes appear. Some have very desirable properties. Others do not, at least for our purposes. Here, the possibility of simultaneous arrivals of both photons to one or the other party occurs on average half the time. Now, that might be useful. It's sharable information, but it conflicts with the efficacy of another protocol that allows unambiguous information sharing between the legitimate users. To ensure unambiguous information sharing in a perfect world between the two legitimate users, Alice and Ralph, those measurements are discarded. This reduces the throughput by 50%. A similar situation occurs in traditional BB84 and Ekert91 under basis reconciliation.

Appendix 5.B outlines a transformation on 5.14, where approximate states are derived. These states are those arising in the first two terms in (5.13) and then (5.14). The transformation of the state output by the PBS, truncated and renormalized is shown below. To denote that they arise in a transformation, we call the erstwhile port/path 2, path 'a,' and port/path 3, 'b,' and constrain the angles the users can measure polarization with to be exactly the same. The common angle $\delta = \theta_a + \theta_b$ and $\theta_a = \theta_b$. The reduced state is,

$$|d_{out}\rangle = \frac{\cos(2\delta)}{\sqrt{2}}\left(\left|\Psi_1\left(ha;vb\mid vb;ha\right)\right\rangle + \left|\Psi_1\left(hb;va\mid va;hb\right)\right\rangle\right)$$
$$+\frac{\sin(2\delta)}{\sqrt{2}}\left(\left|\Psi_3\left(ha;hb\mid va;vb\right)\right\rangle + \left|\Psi_3\left(hb;ha\mid vb;va\right)\right\rangle\right)$$

(5.15a)

$$|d_{out}\rangle = \frac{\cos(2\delta)}{\sqrt{2}}\left(\left|\Psi_1^{(195)}\left(11;00\mid00;11\right)\right\rangle + \left|\Psi_1^{(150)}\left(10;01\mid01;10\right)\right\rangle\right)$$
$$+\frac{\sin(2\delta)}{\sqrt{2}}\left(\left|\Psi_3^{(228)}\left(11;10\mid01;00\right)\right\rangle + \left|\Psi_3^{(177)}\left(10;11\mid00;01\right)\right\rangle\right)$$

(5.15b)

$$|d_{out}\rangle = \frac{\cos(2\delta)}{\sqrt{2}}\left(\left|\Psi_1^{(195)}\right\rangle + \left|\Psi_1^{(150)}\right\rangle\right) + \frac{\sin(2\delta)}{\sqrt{2}}\left(\left|\Psi_3^{(228)}\right\rangle + \left|\Psi_3^{(177)}\right\rangle\right) \tag{5.15c}$$

Defined in Appendix 5.A, the Bell forms are not unique in the sense that they were constructed arbitrarily by collecting terms resulting from the transformation producing (5.15). The amplitudes arising in that transformation do split up into distinct Bell form classes, but the amplitudes within a class were collected and summed by arbitrary choice. Be that as it may, once chosen they can be represented uniquely by binary bit strings, which can then be expressed in base ten. Here, h->1, v->0, a->1, b->0. The '|' symbol between the degrees of freedom denote + or -, depending on the particular Bell form in which they are ensconced. In this condensed notation, ';' divides the two subspaces that are entangled. The superscript on the Ψ Bell forms is the base 10 representation of the concatenated degrees of freedom expressed as a binary stream. Finally, the subscript identifies a particular Bell form.

An interpretation of (5.15) is that the composite system is behaving like a single system possessing four possible states, two per Bell form class, and all transporting entanglement. In the absence of decohering processes, this obtains even when the two spatial modes of the system splay the parts of the system extensively over space-time.

To compute the density matrix of the output state, we encode the constituent basis elements in (5.15) by their internal degrees of freedom.

$$\rho_\Psi = \frac{1}{4}\begin{bmatrix}
 & vb;va & vb;ha & va;vb & va;hb & hb;va & hb;ha & ha;vb & ha;hb & \\
 & 0001 & 0011 & 0100 & 0110 & 1001 & 1011 & 1100 & 1110 & \\
 & 1 & 3 & 4 & 6 & 9 & 11 & 12 & 14 & \\
 & s^2 & -cs & s^2 & -cs & -cs & -s^2 & -cs & -s^2 & 1 \\
 & -cs & c^2 & -cs & c^2 & c^2 & cs & c^2 & cs & 3 \\
 & s^2 & -cs & s^2 & -cs & -cs & -s^2 & -cs & -s^2 & 4 \\
 & -cs & c^2 & -cs & c^2 & c^2 & cs & c^2 & cs & 6 \\
 & -cs & c^2 & -cs & c^2 & c^2 & cs & c^2 & cs & 9 \\
 & -s^2 & cs & -s^2 & cs & cs & s^2 & cs & s^2 & 11 \\
 & -cs & c^2 & -cs & c^2 & c^2 & cs & c^2 & cs & 12 \\
 & -s^2 & cs & -s^2 & cs & cs & s^2 & cs & s^2 & 14
\end{bmatrix} \tag{5.16}$$

Symbol 'c' stands for cosine, and symbol 's' for sine. This 8X8 matrix contains 64 elements. It is a reduced dimension version of the full system matrix, a 16X16 that included the discarded terms. The full system matrix, including the discarded terms is displayed in Appendix 5.D. Possessing a trace equal to one (5.16) is a proper density operator. Moreover, its square equals itself, so it describes a pure state. Its eigenvalues are the set $\{0,0,0,0,0,0,0,1\}$.

One measure of whether a state is entangled is obtained by forming the partial transpose of a density operator purporting to represent a separable state. If the density operator of a two particle composite system is a tensor product of independent density operators, and each density operator necessarily has non-negative eigenvalues, as do their transposes, the tensor product of the two density operators will also have non-negative eigenvalues. *Necessarily, so will the density operator of the tensor product of one system with the transpose of the other.* That means the density operator is separable as a tensor

product of two proper density operators. However, if the eigenvalues of the partially transposed density operator of a composite system has at least one negative eigenvalue, it is not separable. Its density operator cannot be represented by a sum of tensor products of two qubits. It is an entangled system.

$$
\rho_\Psi^{PT} = \frac{1}{4}
\begin{array}{cccccccc}
vb;va & vb;ha & va;vb & va;hb & hb;va & hb;ha & ha;vb & ha;hb \\
0001 & 0011 & 0100 & 0110 & 1001 & 1011 & 1100 & 1110 \\
1 & 3 & 4 & 6 & 9 & 11 & 12 & 14 \\
\end{array}
\left[
\begin{array}{cccccccc|c}
s^2 & -cs & s^2 & -cs & -cs & c^2 & -cs & c^2 & 1 \\
-cs & c^2 & -cs & c^2 & -s^2 & cs & -s^2 & cs & 3 \\
s^2 & -cs & s^2 & -cs & -cs & c^2 & -cs & c^2 & 4 \\
-cs & c^2 & -cs & c^2 & -s^2 & cs & -s^2 & cs & 6 \\
-cs & -s^2 & -cs & -s^2 & c^2 & cs & c^2 & cs & 9 \\
c^2 & cs & c^2 & cs & cs & s^2 & cs & s^2 & 11 \\
-cs & -s^2 & -cs & -s^2 & -s^2 & cs & c^2 & cs & 12 \\
c^2 & cs & c^2 & cs & cs & s^2 & cs & s^2 & 14 \\
\end{array}
\right]
\qquad (5.17)
$$

The partial transpose of (5.16) is displayed in (5.17). Its eigenvalues are the set $\{0,\,0,0,0,\,-1/2,\,1/2,\,1/2,\,1/2\}$. Therefore, because at least one eigenvalue is negative, the reduced constituent amplitude density matrix representation of the composite system exiting the PBS, (5.16), represents an entangled system. This is independent of angle δ.

The partial transpose technique for determining separability originated with Asher Peres [10], and its limitations were quantified by the Horodeckis [11,12]. Unfortunately, the method is not scalable in the sense that some density matrices of higher dimension than 2X2 and 2X3, known to be non-separable, do not possess any negative eigenvalues. That situation has been termed bound entanglement. The Horodeckis determined that the Peres criterion is necessary to prove non-separability, but is not sufficient.

It is interesting to trace out degrees of freedom from both sub-systems in an effort to ascertain what degrees of freedom, if any, are left entangled. In this model, the frequency degree of freedom is associated with a particular ket in the ordering of the entangled state, as discussed below (5.1). Hence we will suppress its symbol within the kets, keeping their order or simply denoting the internal degrees of freedom associated with a particular frequency, f1 or f2, by '1' and '2' subscripts. Recalling (5.15),

$$
\left| d_{out} \right\rangle = \frac{\cos(2\delta)}{\sqrt{2}} \left(\left| \Psi_1^{(195)} \right\rangle + \left| \Psi_1^{(150)} \right\rangle \right) + \frac{\sin(2\delta)}{\sqrt{2}} \left(\left| \Psi_3^{(228)} \right\rangle + \left| \Psi_3^{(177)} \right\rangle \right), \qquad (5.18)
$$

Its composite state density operator can be written as,

$$\rho_\Psi = \frac{\cos^2(2\delta)}{2}\left(\left|\Psi_1^{(195)}\right\rangle\left\langle\Psi_1^{(195)}\right| + \left|\Psi_1^{(195)}\right\rangle\left\langle\Psi_1^{(150)}\right| + \left|\Psi_1^{(150)}\right\rangle\left\langle\Psi_1^{(195)}\right| + \left|\Psi_1^{(150)}\right\rangle\left\langle\Psi_1^{(150)}\right|\right)$$

$$+\frac{\cos(2\delta)\sin(2\delta)}{2}\left(\begin{array}{c}\left|\Psi_1^{195}\right\rangle\left\langle\Psi_3^{228}\right| + \left|\Psi_1^{150}\right\rangle\left\langle\Psi_3^{228}\right| + \left|\Psi_1^{195}\right\rangle\left\langle\Psi_3^{177}\right| + \left|\Psi_1^{150}\right\rangle\left\langle\Psi_3^{177}\right| \\ + \left|\Psi_3^{228}\right\rangle\left\langle\Psi_1^{195}\right| + \left|\Psi_3^{228}\right\rangle\left\langle\Psi_1^{150}\right| + \left|\Psi_3^{177}\right\rangle\left\langle\Psi_1^{195}\right| + \left|\Psi_3^{177}\right\rangle\left\langle\Psi_1^{150}\right|\end{array}\right) \tag{5.19}$$

$$+\frac{\sin^2(2\delta)}{2}\left(\left|\Psi_3^{228}\right\rangle\left\langle\Psi_3^{228}\right| + \left|\Psi_3^{228}\right\rangle\left\langle\Psi_3^{177}\right| + \left|\Psi_3^{177}\right\rangle\left\langle\Psi_3^{228}\right| + \left|\Psi_3^{177}\right\rangle\left\langle\Psi_3^{177}\right|\right)$$

We then compute the partial traces over the different degrees of freedom within the states, i.e., $\text{Tr}_{(\_x;\_y)}(\rho_\Psi)$ and $\text{Tr}_{(x\_;y\_)}(\rho_\Psi)$. The first is a partial trace over path and the second a partial trace over polarization.

$$\text{Tr}_{(\_x;\_y)}(\rho_\Psi) = \left\langle a_1 a_2 \left|\rho_\Psi\right| a_1 a_2\right\rangle + \left\langle a_1 b_2 \left|\rho_\Psi\right| a_1 b_2\right\rangle + \left\langle b_1 a_2 \left|\rho_\Psi\right| b_1 a_2\right\rangle + \left\langle b_1 b_2 \left|\rho_\Psi\right| b_1 b_2\right\rangle \tag{5.20a}$$

$$\text{Tr}_{(x\_;y\_)}(\rho_\Psi) = \left\langle h_1 h_2 \left|\rho_\Psi\right| h_1 h_2\right\rangle + \left\langle h_1 v_2 \left|\rho_\Psi\right| h_1 v_2\right\rangle + \left\langle v_1 h_2 \left|\rho_\Psi\right| v_1 h_2\right\rangle + \left\langle v_1 v_2 \left|\rho_\Psi\right| v_1 v_2\right\rangle \tag{5.20b}$$

Tracing over path degrees of freedom renders the reduced density matrix in polarization degrees of freedom, (5.20a). It can be constructed by reference to (5.16) and look for terms consistent with (5.20a). In the same basis used in (5.20a), the reduced density matrix for polarization is,

$$\rho_{pol} = \frac{1}{4}\begin{array}{c}\begin{array}{cccccccc} v;v & v;h & v;v & v;h & h;v & h;h & h;v & h;h \\ 0001 & 0011 & 0100 & 0110 & 1001 & 1011 & 1100 & 1110 \\ 00 & 01 & 00 & 01 & 10 & 11 & 10 & 11 \end{array} \\ \left[\begin{array}{cccccccc} s^2 & -cs & 0 & 0 & -cs & -s^2 & 0 & 0 \\ -cs & c^2 & 0 & 0 & c^2 & cs & 0 & 0 \\ 0 & 0 & s^2 & -cs & 0 & 0 & -cs & -s^2 \\ 0 & 0 & -cs & c^2 & 0 & 0 & c^2 & cs \\ -cs & c^2 & 0 & 0 & c^2 & cs & 0 & 0 \\ -s^2 & cs & 0 & 0 & cs & s^2 & 0 & 0 \\ 0 & 0 & -cs & c^2 & 0 & 0 & c^2 & cs \\ 0 & 0 & -s^2 & cs & 0 & 0 & cs & s^2 \end{array}\right]\begin{array}{c} 00 \\ 01 \\ 00 \\ 01 \\ 10 \\ 11 \\ 10 \\ 11 \end{array}\end{array} \tag{5.21}$$

We have written the binary reductions beneath the former binary bases, having traced out the red bits which denoted the path, leaving polarization degrees of freedom intact. Note there exists just four unique bases in the reduced basis set. Two rows are multiples of two other rows in (5.21). This causes

degeneracy in the eigenvalue spectrum. Eigenvalues of (5.21) are the set {0,0,0,0,0,0,1/2,1/2}. Its partial transpose is

$$
\rho_{\text{pol}}^{\text{PT}} = \frac{1}{4}
\begin{array}{c}
\begin{array}{cccccccc}
v;v & v;h & v;v & v;h & h;v & h;h & h;v & h;h \\
0001 & 0011 & 0100 & 0110 & 1001 & 1011 & 1100 & 1110 \\
00 & 01 & 00 & 01 & 10 & 11 & 10 & 11
\end{array} \\
\left[
\begin{array}{cccccccc}
s^2 & -cs & 0 & 0 & -cs & c^2 & 0 & 0 \\
-cs & c^2 & 0 & 0 & -s^2 & cs & 0 & 0 \\
0 & 0 & s^2 & -cs & 0 & 0 & -cs & c^2 \\
0 & 0 & -cs & c^2 & 0 & 0 & -s^2 & cs \\
-cs & -s^2 & 0 & 0 & c^2 & cs & 0 & 0 \\
c^2 & cs & 0 & 0 & cs & s^2 & 0 & 0 \\
0 & 0 & -cs & -s^2 & 0 & 0 & c^2 & cs \\
0 & 0 & c^2 & cs & 0 & 0 & cs & s^2
\end{array}
\right]
\begin{array}{c}
00 \\ 01 \\ 00 \\ 01 \\ 10 \\ 11 \\ 10 \\ 11
\end{array}
\end{array}
\qquad (5.22)
$$

Matrix (5.22) has two negative eigenvalues in the set {-1/4, -1/4, 1/4, 1/4, 1/4, 1/4, 1/4, 1/4}. Hence the reduced density in polarization necessarily describes an entangled state. It reduces to (5.23), on the left. Its partial transpose is on the right. Respectively, their eigenvalues are {0,0,0,1} and (-1/2,1/2,1/2,1/2). Compare these eigenvalues with those found for (5.16), (5.17), and for the full system density matrix in Appendix 5.C.

$$
\rho_{\text{rpol}} = \frac{1}{2}
\begin{array}{c}
\begin{array}{cccc}
v_1v_2 & v_1h_2 & h_1v_2 & h_1h_2 \\
00 & 01 & 10 & 11
\end{array} \\
\left[
\begin{array}{cccc}
s^2 & -cs & -cs & -s^2 \\
-cs & c^2 & c^2 & cs \\
-cs & c^2 & c^2 & cs \\
-s^2 & cs & cs & s^2
\end{array}
\right]
\begin{array}{c}
00 \\ 01 \\ 10 \\ 11
\end{array}
\end{array}
\qquad
\rho_{\text{rpol}}^{\text{pt}} = \frac{1}{2}
\begin{array}{c}
\begin{array}{cccc}
v_1v_2 & v_1h_2 & h_1v_2 & h_1h_2 \\
00 & 01 & 10 & 11
\end{array} \\
\left[
\begin{array}{cccc}
s^2 & -cs & -cs & c^2 \\
-cs & c^2 & -s^2 & cs \\
-cs & -s^2 & c^2 & cs \\
c^2 & cs & cs & s^2
\end{array}
\right]
\begin{array}{c}
00 \\ 01 \\ 10 \\ 11
\end{array}
\end{array}
\qquad (5.23)
$$

ρ_{rpol} *is* pure, for it equals its square. The partial transpose has one negative eigenvalue. Polarization entanglement is maintained, and over all common measurement angles performed by nodes a and b.

Returning to (5.16) we now trace over the polarization degrees of freedom according to the prescription in (5.20b).

$$
\rho_{\text{path}} = \frac{1}{4}
\begin{array}{c}
\begin{array}{cccccccc}
b;a & b;a & a;b & a;b & b;a & b;a & a;b & a;b \\
0001 & 0011 & 0100 & 0110 & 1001 & 1011 & 1100 & 1110 \\
01 & 01 & 10 & 10 & 01 & 01 & 10 & 10
\end{array}\\
\left[\begin{array}{cccccccc}
s^2 & 0 & s^2 & 0 & 0 & 0 & 0 & 0 \\
0 & c^2 & 0 & c^2 & 0 & 0 & 0 & 0 \\
s^2 & 0 & s^2 & 0 & 0 & 0 & 0 & 0 \\
0 & c^2 & 0 & c^2 & 0 & 0 & 0 & 0 \\
0 & 0 & 0 & 0 & c^2 & 0 & c^2 & 0 \\
0 & 0 & 0 & 0 & 0 & s^2 & 0 & s^2 \\
0 & 0 & 0 & 0 & c^2 & 0 & c^2 & 0 \\
0 & 0 & 0 & 0 & 0 & s^2 & 0 & s^2
\end{array}\right]
\begin{array}{c}
01\\01\\10\\10\\01\\01\\10\\10
\end{array}
\end{array}
\tag{5.24}
$$

The partial transpose of (5.24) is,

$$
\rho_{\text{path}}^{PT} = \frac{1}{4}
\begin{array}{c}
\begin{array}{cccccccc}
b;a & b;a & a;b & a;b & b;a & b;a & a;b & a;b \\
0001 & 0011 & 0100 & 0110 & 1001 & 1011 & 1100 & 1110 \\
01 & 01 & 10 & 10 & 01 & 01 & 10 & 10
\end{array}\\
\left[\begin{array}{cccccccc}
s^2 & 0 & s^2 & 0 & 0 & 0 & 0 & 0 \\
0 & c^2 & 0 & c^2 & 0 & 0 & 0 & 0 \\
s^2 & 0 & s^2 & 0 & 0 & 0 & 0 & 0 \\
0 & c^2 & 0 & c^2 & 0 & 0 & 0 & 0 \\
0 & 0 & 0 & 0 & c^2 & 0 & c^2 & 0 \\
0 & 0 & 0 & 0 & 0 & s^2 & 0 & s^2 \\
0 & 0 & 0 & 0 & c^2 & 0 & c^2 & 0 \\
0 & 0 & 0 & 0 & 0 & s^2 & 0 & s^2
\end{array}\right]
\begin{array}{c}
01\\01\\10\\10\\01\\01\\10\\10
\end{array}
\end{array}
= \rho_{\text{path}}
\tag{5.25}
$$

In the current configuration, the reduced density matrix for path equals its partial transpose. Their eigenvalues are $\{0,0,0,0,\dfrac{\cos^2(2\delta)}{2},\dfrac{\cos^2(2\delta)}{2},\dfrac{\sin^2(2\delta)}{2},\dfrac{\sin^2(2\delta)}{2}\}$. These eigenvalues are always positive. If we put the frequency degrees of freedom explicitly back into the bases, though it was always there implicitly in the ordering and identification of the kets as 1 and 2, nothing changes. Frequency/path is still a mixed state in its reduced density after the polarization has been removed. Correlations exist, but not entanglement between those degrees of freedom. The Lyot stack acts on frequency states to either change their polarization or leave it effectively invariant. The PBS projects those states into different paths, depending on their polarization. Under the current configuration, polarization is the entanglement carrier within the extant degrees of freedom. That does not necessarily

mean that path and polarization and frequency are not entangled in the joint distribution. (5.16) proves otherwise.

Returning to (5.25), we see that there exist just two unique basis elements: (a;b) and (b;a). This means that frequency f_1 will appear at port (a) P_2, or (b) P_3, with equal probability. Similarly, frequency f_2 appears at either port. But that coincidence does not mean that path and frequency are entangled. They are correlated, but not entangled *in the reduced matrix representation of the system*. Moreover, the reduced density matrix for path and frequency does not equal its square. It is not a pure state. However, had we included the full set of possibilities, the two photon coincidence states, path and frequency remain entangled, i.e.,

$$
\rho_{\text{rpath}} = \frac{1}{2}
\begin{bmatrix}
 & \text{b;b} & \text{b;a} & \text{a;b} & \text{a;a} \\
0 & 0 & 0 & 0 \\
0 & 1 & 1 & 0 \\
0 & 1 & 1 & 0 \\
0 & 0 & 0 & 0
\end{bmatrix}
\quad
\rho_{\text{rpath}}^{\text{PT}} = \frac{1}{2}
\begin{bmatrix}
 & \text{b;b} & \text{b;a} & \text{a;b} & \text{a;a} \\
0 & 0 & 0 & 1 \\
0 & 1 & 0 & 0 \\
0 & 0 & 1 & 0 \\
1 & 0 & 0 & 0
\end{bmatrix}
\qquad (5.26)
$$

(5.26) *is* a pure state, and its partial transpose *does* possess a negative eigenvalue.

Another measure of entanglement, different from the negativity in the partial transpose eigenvalue spectrum of the constituent particle system density matrix, is the comparison of probabilities one would get if the system were classical and separable with those probabilities computed using quantum mechanics. The concept was introduced by John Bell [13] in response to Einstein, Podolsky, and Rosen's conjecture that quantum mechanics is incomplete; it did not explain correlations between non-interacting particles possessing observables simultaneously measured in an inertial reference frame and the two parties separated by space like metric distances [14]. The particles in question, EPR argue, possess real properties even in the absence of measurement, and that no connection between the particles can exist that can propagate at speeds greater than that of light in vacuum such that measurements on one affect outcomes of the other. Bell's theorem argues against the validity of EPR's assumptions on local realism, that quantum systems possess definite values, and that quantum mechanics predicts the outcome of correlation experiments, whereas classical statistical mechanics cannot. His concept has been extended by several researchers, such as Clauser, Horne, Shimony, and Holt [15] who formulated the CHSH inequality. See Appendix 5.C, where we compute the so-called CHSH inequality following a prescription given by Stenholm and Suominen [16].

5.4   Quantum Key Distribution

Returning now to (5.15a), we expand it to make explicit the degrees of freedom and their structural relationship.

$$
\left| d_{\text{out}} \right\rangle = \frac{\cos(2\delta)}{\sqrt{2}} \left(\left| \Psi_1^{195} \right\rangle + \left| \Psi_1^{150} \right\rangle \right) + \frac{\sin(2\delta)}{\sqrt{2}} \left(\left| \Psi_3^{228} \right\rangle + \left| \Psi_3^{177} \right\rangle \right)
\qquad (5.27a)
$$

$$\left|d_{out}\right\rangle = \frac{\cos(2\delta)}{\sqrt{2}}\left(\left|\Psi_1\left(11;00\,|\,00;11\right)\right\rangle + \left|\Psi_1\left(10;01\,|\,01;10\right)\right\rangle\right)$$
$$+\frac{\sin(2\delta)}{\sqrt{2}}\left(\left|\Psi_3\left(11;10\,|\,01;00\right)\right\rangle + \left|\Psi_3\left(10;11\,|\,00;01\right)\right\rangle\right)$$

(5.27b)

$$=\frac{\cos(2\delta)}{2}\left(\left|ha;vb+vb;ha\right\rangle + \left|hb;va+va;hb\right\rangle\right)$$
$$+\frac{\sin(2\delta)}{2}\left(\left|ha;hb-va;vb\right\rangle + \left|hb;ha-vb;va\right\rangle\right)$$

(5.27c)

Choosing the PBS basis, $\delta=0$, and having agreed to discard two photon coincidence per node events, polarization measurements at 'a' and 'b' are 100% anti-correlated. Choosing the alternative basis, $\delta=p/4$, polarization measurements are 100% correlated.

Polarization measurements performed by parties at 'a' and at 'b', call them Alice and Ralph, yielding two photon events can be discarded. That amounts to an average 50% reduction in throughput. It happens in BB84 when Alice randomly chooses a basis from two, two dimensional bases in which to send a photon, and Ralph independently and randomly measures in one of the two, bases. They retain only those bases that coincide, on average 50% of the time. Here, however, even when they have chosen to stick with two possible bases differing by 45°, they would still have to reconcile their choices. That is, if they choose those bases at random and independently, half the time their choices would agree and half the time not. That's a total reduction in throughput to 25%. This can be avoided. If they share a secret key allowing them to select predetermined bases, basis reconciliation is unnecessary [17]. That key can be generated by a classical stream cipher possessing enormous mathematical complexity. To generate long running keys, all it needs is a secret seed key. That might be obtainable, at least in principle, by QKD.

Table 10 summarizes the ideal results two possibly displaced users would measure on the composite state after discarding two photon arrivals per port, and when the input state utilized is,

$$\left|a_{in}\right\rangle = \frac{1}{2}\left(\left|H_1P_1;H_2P_1+V_1P_1;V_2P_1\right\rangle + \left|H_1P_4;H_2P_4\,|\,V_1P_4;V_2P_4\right\rangle\right)$$

(5.28)

Table 10 Polarization Measurements by Two Displaced Users

	$\delta=0$		$\delta=\pi/4$	
Alice	H	V	h	v
Ralph	V	H	h	v

5.5 Conclusion

Designed for wavelength division multiplexing of classical electromagnetic optical beams, the Lyot stack employs birefringence to discriminate between frequencies of incoming states. Their optical path length (OPD) phases differ when passing through an engineered thickness. Those frequencies whose OPD phase is an integral multiple of 2π upon exit from the stack are termed congruent frequencies. Frequencies whose OPD phase is an odd integral of π are termed incongruent frequencies. Polarization states of congruent frequencies are left invariant, while those of incongruent states are rotated by $\pi/2$. After exiting the Lyot stack, the two frequencies are split into different output paths for further

processing. This allows multiple access to a hub whose spokes are geographically displaced. An obvious application is reception and dissemination of ISR data collected by the spokes, sent to the hub, and transported either by satellite cross links or by direct linkage from satellite to another location not accessible by the spokes.

Our in-house 6.1 basic work thus far focused on attempting to test the hypothesis that polarization entanglement of a rotationally invariant entangled quantum state is not preserved in transit through a perfect birefringent spectral filter stage. In the current model, our analysis has shown that, with modification, polarization entanglement is preserved in the joint state as it transits through a perfect birefringent spectral filter stage comprised of a Lyot stack followed by a polarization beam splitter.

Initial polarization entanglement is maintained through the Lyot stack, but is changed from a rotationally invariant entangled state to a non-rotationally invariant state. Passage through the PBS still maintains polarization entanglement in the joint state. In the joint state, polarization is entangled with path. One modification ensuring this is a purification operation allowing the possibility that the state enters not one, but two ports. This is accomplished physically by placing a non-polarizing beam splitter in the entrance path to the Lyot stage. The state exiting the PBS is then transformed to a linear combination of pure states allowing users to execute polarization measurements in either the PBS basis or the Lyot filter basis rotated by 45°. This capability comes at a cost. Cross terms from the BS transformation also enter the Lyot stage, and they produce the possibility of two photon coincidence events at each PBS output port. If the users discard those two photon coincident events, polarization measurements in the PBS basis are 100% anti-correlated, while measurements in the Lyot stack basis are %100 correlated. This incurs on average a 50% reduction in throughput. Of course, the users may wish to use the discarded events.

Experimental results in the literature indicate path and frequency can become entangled [18]. If *the BS is removed from the collinear input, only one entry port is available*. After passing through the Lyot stack, f1 and f2 randomly exit either P_2/(a) or P_3/(b), but always at different ports. They do so because the exit state from the PBS is $|HP_2; VP_3>+|VP_3; HP_2>$; polarization H always goes out P_2, and polarization V always goes out P_3. Frequencies associated with the particular polarization states follow. A measurement of frequency allows Alice to infer Ralph's frequency. On that basis, information is shared. How securely that information is shared will likely require a buttressing protocol, perhaps involving shared time bin detection [19].

A temporal delay will occur when an eavesdropper intercepts, then detects the frequency for exploitation, before sending that photon on its way to the legitimate user. Accurate and precise time binning might be able to detect that temporal delay and indicate the intrusion compromising the confidentiality of the shared information. In that case, one needs only to flip the logic value assigned to the frequency. That simple operation imparts a coin flip guess on its value to the eavesdropper. Furthermore, there is no need to maintain a common rotation angle, δ, for polarization measurements. Availability is more robust.

Simpler methods exist for this type of information sharing, protocols preferred by engineers tasked to get the job done with optimal information confidentiality, integrity, and availability. Our interest in the current Lyot stage device characteristics goes beyond QKD. A future report will convey details.

References

[1] NuCrypt LLC, *Novel Protocol for Quantum Key Distribution*, Contract FA8750-12-C-0241.

[2] Optical Physics Company, *Compact Multi-Access Lasercom*, Contract FA8750-11-C-0163.

[3] Richard A. Hutchins,"Birefringent Spectral Filter", Optical Physics Company PATENT, US7400448 B2 (granted 2008).

[4] S.X Wang, Gregory Kanter, "Robust Multiwavelength All-Fiber Source of Polarization-Entangled Photons with Built-In Analyzer Signal," IEEE Journ Select. Topics Quant. Elec., Vol. 15, Iss. 6, pp. 1733, (2009).

[5] S.X. Wang, et al., "Fast Measurement of Entangled Photons," JLT, Vol. 31, Iss. 5, pp: 707-714, (2013).

[6] Edward Collett, *Polarized Light, Fundamentals and Applications*, Marcel Dekker, (1993); Dennis Goldstein, *Polarized Light*, CRC Press (2010).

[7] Ulf Leonhardt, "Quantum physics of simple optical instruments," Rep. Prog. Phys., Vol. 66, (2003) & quant-ph/0305007v2.

[8] Ulf Leonhardt, *Measuring the Quantum State of Light*, Cambridge University Press, ISBN-13: 978-0521023528, (2005).

[9] Christopher C. Gerry, and Peter L. Knight "Introductory Quantum Optics," Cambridge University Press, (2006).

[10] Asher Peres, "Separability Criterion for Density Matrices," Phys. Rev. Lett., Vol. 77, No. 8, 1413 (1996).

[11] Horodecki, Horodecki, and Horodecki, "Separability of Mixed Quantum States," Physics Letters A, Vol. 223, pp 1-8,(1996).

[12] Horodecki, Horodecki, Horodecki, and Horodecki, "Quantum Entanglement," Rev. Mod. Phys., Vol. 81, April-June, 865, (2009).

[13] John Bell, "On the Einstein, Podolsky, Rosen Paradox," Physics, Vol. 1, No. 3, pp. 195-200, (1964).

[14] A. Einstein, B. Podolsky, and N. Rosen, "Can Quantum-Mechanical Description of Physical Reality be Considered Complete?" Phys. Rev., Volume 47, p. 777, (1935).

[15] J. Clauser, M. Horne, A. Shimony, and R. Holt, "Proposed Experiment to Test Local Hidden-Variable Theories," Phys. Rev. Lett. Vol. 23, No. 15, p. 880, (1969).

[16] S. Stenholm, K-A Suominen, *Quantum Approach to Informatics*, Wiley, ISBN-13 978-0-471-73610-3, pp. 46-49, (2005).

[17] Horace Yuen, "Key Generation,: Foundations and a New Quantum Approach," IEEE Journ. Select. Topics in Quant. Elect., Vol. 15, No. 6, pp 1630-1645, (2009).

[18] R. Ramelow et al, "Discrete Tunable Color Entanglement," Phys. Rev. Lett., Vol. 103, 253601 (2009).

[19] R. Erdmann, D.H. Hughes, R. Michalak, J. Malowicki, P. Cook, "The Uncertainty Principle and entangled correlations in quantum key distribution protocols,' SPIE Proceedings: Defense-Security 9123-2 (2013).

Appendix 5.A Generalized Bell Forms

A general bipartite combination of two states in the Jordan-Schwinger representation is given by,

$$|\Psi\rangle = \left[\,|x_1\rangle \;\; |w_1\rangle\,\right] \; R \bullet \sigma \begin{bmatrix} |y_2\rangle \\ |z_2\rangle \end{bmatrix} = \left[\,|x_1\rangle \;\; |w_1\rangle\,\right] \begin{bmatrix} R_0 + R_3 & R_1 - iR_2 \\ R_1 + iR_2 & R_0 - R_3 \end{bmatrix} \begin{bmatrix} |y_2\rangle \\ |z_2\rangle \end{bmatrix}$$

$$= \left(R_0 + R_3\right)|x_1\rangle|y_2\rangle + \left(R_1 - iR_2\right)|x_1\rangle|z_2\rangle + \left(R_1 + iR_2\right)|w_1\rangle|y_2\rangle + \left(R_0 - R_3\right)|w_1\rangle|z_2\rangle \quad \text{(5.A. 1)}$$

$$\Box \; \Psi_{R_0,R_1,R_2,R_3} \left\{\{x_1, w_1\}, \{y_2, z_2\}\right\}$$

For $R_0 = \frac{1}{\sqrt{2}}$ and $R_1 = R_2 = R_3 = 0$, and the degrees of freedom carried by the state, $(\,x_1; z_2 \mid w_1 y_2$ where the semicolon differentiates between the two spaces,

$$\left|\Psi_{\frac{1}{\sqrt{2}},0,0,0}\right\rangle = \frac{1}{\sqrt{2}}\left(|x_1\rangle|y_2\rangle + |w_1\rangle|z_2\rangle\right) \;\Box\; |\Psi_0\rangle \qquad \text{(5.A.2)}$$

Similarly,

$$\left|\Psi_{0,\frac{1}{\sqrt{2}},0,0}\right\rangle = \frac{1}{\sqrt{2}}\left(|x_1\rangle|z_2\rangle + |w_1\rangle|y_2\rangle\right) \;\Box\; |\Psi_1\rangle \qquad \text{(5.A.3)}$$

$$\left|\Psi_{0,0,\frac{i}{\sqrt{2}},0}\right\rangle = \frac{1}{\sqrt{2}}\left(|x_1\rangle|z_2\rangle - |w_1\rangle|y_2\rangle\right) \;\Box\; |\Psi_2\rangle \qquad \text{(5.A.4)}$$

$$\left|\Psi_{0,0,0,\frac{1}{\sqrt{2}}}\right\rangle = \frac{1}{\sqrt{2}}\left(|x_1\rangle|y_2\rangle - |w_1\rangle|z_2\rangle\right) \;\Box\; |\Psi_3\rangle \qquad \text{(5.A.5)}$$

In the Lyot stack reference frame, the Lyot stack changes the entangled (5.A.2) state to the entangled (5.A.5) state. The transformation in Appendix 5.b recovers this last as part of the pure state derived there as a linear combination of Bell state forms in the PBS frame and the Lyot frame.

$$L_1 R_{\frac{1}{\sqrt{2}},0,0,0} L_2^{\dagger} = i\sigma_1 \frac{\sigma_0}{\sqrt{2}}(-i)\sigma_2^{\dagger} = -i\frac{\sigma_3}{\sqrt{2}} \qquad \text{(5.A.6)}$$

Hence, in the Lyot stack frame, diagonal to the PBS frame,

$$|\Psi\rangle = \left[\; |h_1\rangle \;\; |v_1\rangle \;\right] \; L_1 R_{\frac{1}{\sqrt{2}},0,0,0} \; L_2^{\dagger} \begin{bmatrix} |h_2\rangle \\ |v_2\rangle \end{bmatrix}$$

$$= \left[\; |h_1\rangle \;\; |v_1\rangle \;\right] \begin{bmatrix} -i\dfrac{1}{\sqrt{2}} & 0 \\[2mm] 0 & i\dfrac{1}{\sqrt{2}} \end{bmatrix} \begin{bmatrix} |h_2\rangle \\ |v_2\rangle \end{bmatrix} \qquad (5.A.7)$$

$$= -\frac{i}{\sqrt{2}}\left(|h_1\rangle\big)|h_2\rangle - |v_1\rangle|v_2\rangle \right)$$

The state is polarization entangled.

Traditional Bell states usually only consider one degree of freedom. The Bell forms used in this report are orthogonal, even within the same Bell form but carrying different degrees of freedom. Thus these Bell forms are generalizations of traditional Bell states.

Appendix 5.B Transformation of the Composite State
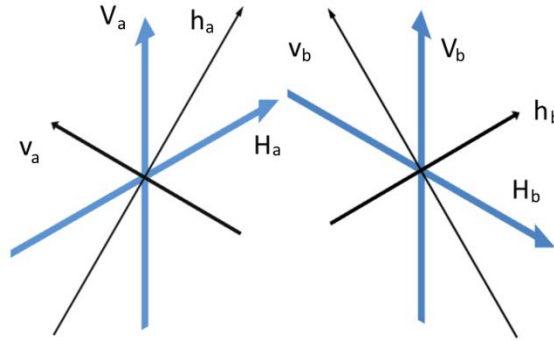
Figure 38 Two coordinates systems related by a $\pi/2$ rotation about a common axis, with local coordinate rotations about their respective propagation directions. P_2-> 'a' and P_3 -> 'b' in the transformed frame.

For convenience, we will use very compact notation. A single state ket and a bipartite ket will be specified in the following ways,

$$\left|\Psi_1\right\rangle = \left|f,h,a\right\rangle_1 = \left|h_1^a\right\rangle \qquad \left|\Psi_{12}\right\rangle = \left|f1,h,a\right\rangle_1\left|f2,v,b\right\rangle_2 = \left|f1,h_1^a\right\rangle\left|f2,v_2^b\right\rangle = \left|h_1^a;v_2^b\right\rangle \qquad (5.B.1)$$

In the PBS frame, with $P_2 \rightarrow a\ P_3 \rightarrow b$, the state exiting the PBS is,

$$\left|c_{out}\right\rangle = \frac{1}{2}\left(\left|\Psi_1\left(f1,(H_1a,V_1b);f2,(H_2a,V_2b)\right)\right\rangle + \left|\Psi_1\left(f1,(H_1b,V_1a);f2,(H_2b,V_2a)\right)\right\rangle\right)$$
$$+\frac{1}{2}\left(\left|\Psi_1\left(f1,(H_1a,V_1b);f2,(H_2b,V_2a)\right)\right\rangle + \left|\Psi_1\left(f1,(H_1b,V_1a);f2,(H_2a,V_2b)\right)\right\rangle\right) \qquad (5.B.2)$$

Note that product of the frequencies are homogeneous throughout, in fact are implicit in the labeling of the kets 1 and 2. Then (5.B.2) is written,

$$\left|c_{out}\right\rangle = \frac{1}{2}\left(\left|f1\right\rangle_1 \otimes \left|f2\right\rangle_2\right)\left(\left|\Psi_1\left((H_1a,V_1b);(H_2a,V_2b)\right)\right\rangle + \left|\Psi_1\left((H_1b,V_1a);(H_2b,V_2a)\right)\right\rangle\right)$$
$$+\frac{1}{2}\left(\left|f1\right\rangle_1 \otimes \left|f2\right\rangle_2\right)\left(\left|\Psi_1\left((H_1a,V_1b);(H_2b,V_2a)\right)\right\rangle + \left|\Psi_1\left((H_1b,V_1a);(H_2a,V_2b)\right)\right\rangle\right) \qquad (5.B.3)$$

Performing arbitrary independent rotations at both output ports to perform measurements of polarization at two displaced positions upon receive gives,

$$|d\rangle = \tfrac{1}{2\sqrt{2}}\left(\left|h_1^a;h_2^b\right\rangle + \left|h_1^b;h_2^a\right\rangle - \left|v_1^a;v_2^b\right\rangle - \left|v_1^b;v_2^a\right\rangle\right)\sin\left(\theta_a+\theta_b\right)$$

$$+\tfrac{1}{2\sqrt{2}}\left(\left|h_1^a;v_2^b\right\rangle + \left|v_1^b;h_2^a\right\rangle + \left|h_1^b;v_2^a\right\rangle + \left|v_1^a;h_2^b\right\rangle\right)\cos\left(\theta_a+\theta_b\right)$$

$$+\tfrac{1}{2\sqrt{2}}\left(\left|h_1^a;v_2^a\right\rangle + \left|v_1^a;h_2^a\right\rangle\right)\cos\left(2\theta_a\right) + \tfrac{1}{2\sqrt{2}}\left(\left|h_1^b;v_2^b\right\rangle + \left|v_1^b;h_2^b\right\rangle\right)\cos\left(2\theta_b\right)$$

$$+\tfrac{1}{2\sqrt{2}}\left(\left|h_1^a;h_2^a\right\rangle - \left|v_1^a;v_2^a\right\rangle\right)\sin\left(2\theta_a\right) + \tfrac{1}{2\sqrt{2}}\left(\left|h_1^b;h_2^b\right\rangle - \left|v_1^b;v_2^b\right\rangle\right)\sin\left(2\theta_b\right)$$

<div align="right">(5.B.4)</div>

We switched to lower case here to denote we are working in the transformed frame. Note the occurrence of photons simultaneously arriving at either 'a' or 'b'. These arise from the mixed terms exiting the BS. The consequence of this two photon coincidence effect is that it presents noise to a particular QKD protocol relying on 100% correlation in one basis, and 100% anticorrelation in a 45° rotated basis.

Though not necessary, If $\theta_a = \theta_b$ and $\theta_a + \theta_b = \delta$, (5.B.4) reduces to,

$$\tfrac{1}{2\sqrt{2}}\left(\begin{array}{c}\left|h_1^a;h_2^b\right\rangle - \left|v_1^a;v_2^b\right\rangle + \left|h_1^b;h_2^a\right\rangle - \left|v_1^b;v_2^a\right\rangle + \\ \left|h_1^a;h_2^a\right\rangle - \left|v_1^a;v_2^a\right\rangle + \left|h_1^b;h_2^b\right\rangle - \left|v_1^b;v_2^b\right\rangle\end{array}\right)\sin\left(2\delta\right)$$

$$+\tfrac{1}{2\sqrt{2}}\left(\begin{array}{c}\left|h_1^a;v_2^b\right\rangle + \left|v_1^b;h_2^a\right\rangle + \left|h_1^b;v_2^a\right\rangle + \left|v_1^a;h_2^b\right\rangle \\ +\left|h_1^a;v_2^a\right\rangle + \left|v_1^a;h_2^a\right\rangle + \left|h_1^b;v_2^b\right\rangle + \left|v_1^b;h_2^b\right\rangle\end{array}\right)\cos\left(2\delta\right)$$

<div align="right">(5.B.5)</div>

Combining the degrees of freedom within the kets into Bell forms, and encoding them as binary strings,

$$|d\rangle = \tfrac{1}{2}\left(\begin{array}{c}\Psi_3(11;10\,|\,01;00) + \Psi_3(10;11\,|\,00;01) + \\ \Psi_3(11;11\,|\,01;01) + \Psi_3(10;10\,|\,00;00)\end{array}\right)\sin\left(2\delta\right)$$

$$+\tfrac{1}{2}\left(\begin{array}{c}\Psi_1(11;00\,|\,00;11) + \Psi_1(10;01\,|\,01;10) + \\ \Psi_1(11;01\,|\,01;11) + \Psi_1(10;00\,|\,00;10)\end{array}\right)\cos\left(2\delta\right)$$

<div align="right">(5.B.6)</div>

Then, taking the entire string of degrees of freedom without the '|' and the ';', place the base 10 equivalent of the result as a superscript to express the states as,

$$= \tfrac{1}{2}\left(\Psi_3^{(228)} + \Psi_3^{(177)} + \Psi_3^{(245)} + \Psi_3^{(160)}\right)\sin\left(2\delta\right)$$

$$+\tfrac{1}{2}\left(\Psi_1^{(195)} + \Psi_1^{(150)} + \Psi_1^{(215)} + \Psi_1^{(130)}\right)\cos\left(2\delta\right)$$

<div align="right">(5.B.7)</div>

This saves space and uniquely expresses the distribution of the degrees of freedom by the Bell forms. The last two terms in each state are cross terms exiting the BS, inducing two photon coincidences per port. If the other terms are projected out, meaning the measurements on the cross terms are removed from consideration, the state of interest for the current application, a particular QKD protocol, is found as follows. Define a projector onto the states of interest,

$$A = \sum_{j,d} \left| \Psi_j^d \right\rangle \left\langle \Psi_j^d \right| \tag{5.B.8}$$

where j ={1,3} and d={228,177,195,150}. Then operate on $\left| c_{out} \right\rangle$ and renormalize, i.e.,

$$\left| e \right\rangle = \frac{A \left| d \right\rangle}{\sqrt{\left\langle d \right| A^\dagger A \left| d \right\rangle}} = \left(\Psi_1^{(195)} + \Psi_1^{(150)} \right) \frac{\cos(2\delta)}{\sqrt{2}} + \left(\Psi_3^{(228)} + \Psi_3^{(177)} \right) \frac{\sin(2\delta)}{\sqrt{2}} \tag{5.B.9}$$

(5.B.9) means Alice and Ralph utilize only those measurements involving the states entering as a whole through P1 and P4 in figure36 and disregard the rest.

Appendix 5.C

The CHSH inequality states that the maximum classically achievable value is two. Following closely an example given in [15], a Bell test, or BT, is the CHSH inequality given in equation (5.C.1.) It is the relationship between expectation values, or mean values of measurements made by 'a' and 'b' on some observable, perhaps the phase induced on polarization states by a phase plate. Classically,

$$BT = \left| E(a_1, b_1) + E(a_2, b_1) + E(a_1, b_2) - E(a_2, b_2) \right| \leq 2 \qquad (5.C.1)$$

Two parties perform ensemble measurements on two observables each. Then they compute the expectation values and insert their results into (5.C.1). The maximum classical value of BT is 2, because the normalized expectation values, computed by a classical probability density function, each achieve a value of 1. If BT is violated by computing the expectation values using quantum mechanical probability amplitudes, quantum correlations exist between the entangled constituents in the probability amplitudes describing the state of the system.

Consider observables, $O_a(\phi_a)$ and $O_b(\phi_b)$, defined as follows,

$$O_a(\phi_a) = \begin{bmatrix} 0 & e^{i\phi_a} \\ e^{-i\phi_a} & 0 \end{bmatrix}_a \quad \text{and} \quad O_b(\phi_b) = \begin{bmatrix} 0 & e^{i\phi_b} \\ e^{-i\phi_b} & 0 \end{bmatrix}_b \qquad (5.C.2)$$

They act only on the polarization degrees of freedom within each Bell form. Nodes 'a' and 'b' make measurements on ϕ_a and ϕ_b respectively. Suppose 'a' and 'b' have agreed to perform their measurements in their respective diagonal bases, i.e., where the observed polarizations are 100% correlated. Using the computational basis to express the polarization states, the expectation values of interest are,

$$E(\phi_a, \phi_b) = \left\langle \Psi_3^{(177)} \right| + \left\langle \Psi_3^{(228)} \left| O_a(\phi_a) O_b(\phi_b) \right| \Psi_3^{(228)} \right\rangle + \left| \Psi_3^{(177)} \right\rangle$$

$$-\frac{1}{2}\left(\begin{bmatrix} 1 & 0 \end{bmatrix}_a \begin{bmatrix} 0 & e^{i\phi_a} \\ e^{-i\phi_a} & 0 \end{bmatrix}_a \begin{bmatrix} 0 \\ 1 \end{bmatrix}_a \right) \times \left(\begin{bmatrix} 1 & 0 \end{bmatrix}_b \begin{bmatrix} 0 & e^{i\phi_b} \\ e^{-i\phi_b} & 0 \end{bmatrix}_b \begin{bmatrix} 0 \\ 1 \end{bmatrix}_b \right)$$

$$-\frac{1}{2}\left(\begin{bmatrix} 0 & 1 \end{bmatrix}_a \begin{bmatrix} 0 & e^{i\phi_a} \\ e^{-i\phi_a} & 0 \end{bmatrix}_a \begin{bmatrix} 1 \\ 0 \end{bmatrix}_a \right) \times \left(\begin{bmatrix} 0 & 1 \end{bmatrix}_b \begin{bmatrix} 0 & e^{i\phi_b} \\ e^{-i\phi_b} & 0 \end{bmatrix}_b \begin{bmatrix} 1 \\ 0 \end{bmatrix}_b \right) \qquad (5.C.3)$$

(4.C.3) reduces to (4.C.4).

$$E(\phi_a, \phi_b) = -\cos(\phi_a + \phi_b) \qquad (5.C.4)$$

For $\phi_a \in \left\{ \dfrac{\pi}{4}, \dfrac{3\pi}{4} \right\}$ and $\phi_b \in \left\{ -\dfrac{\pi}{2}, 0 \right\}$, $\delta = \dfrac{\pi}{4}$,

$$BT = \left| \cos\left(\frac{\pi}{4} - \frac{\pi}{2} \right) + \cos\left(-\frac{\pi}{2} + \frac{3\pi}{4} \right) + \cos\left(\frac{\pi}{4} + 0 \right) - \cos\left(\frac{3\pi}{4} + 0 \right) \right| = 2\sqrt{2} > 2 \qquad (5.C.5)$$

The CSHS inequality is violated. The state possesses non-local correlations.

A similar demonstration holds for the other Bell form states where the users choose the $\delta = 0$ Bell basis forms to measure correlations.

$$O_a(\phi_a)O_b(\phi_b) = \begin{bmatrix} 0 & e^{i\phi_a} \\ e^{-i\phi_a} & 0 \end{bmatrix}_a \begin{bmatrix} 0 & e^{i\phi_b} \\ e^{-i\phi_b} & 0 \end{bmatrix}_b \tag{5.C.6}$$

$$E(\phi_a,\phi_b) = \left\langle \Psi_1^{(195)} \middle| + \left\langle \Psi_1^{(150)} \middle| O_a(\phi_a)O_b(\phi_b) \middle| \Psi_1^{(150)} \right\rangle + \middle| \Psi_1^{(195)} \right\rangle \tag{5.C.7}$$

$$= \frac{1}{2}\left(\begin{bmatrix} (1 & 0) \end{bmatrix}_a \begin{bmatrix} 0 & e^{i\phi_a} \\ e^{-i\phi_a} & 0 \end{bmatrix}_a \begin{bmatrix} 0 \\ 1 \end{bmatrix}_a \right) \times \left(\begin{bmatrix} (0 & 1) \end{bmatrix}_b \begin{bmatrix} 0 & e^{i\phi_b} \\ e^{-i\phi_b} & 0 \end{bmatrix}_b \begin{bmatrix} 1 \\ 0 \end{bmatrix}_b \right) + CC$$

This gives,

$$E(\phi_a,\phi_b) = \cos(\phi_a - \phi_b) \tag{5.C.8}$$

For $\phi_a \in \left\{\dfrac{\pi}{2},\pi\right\}$ and $\phi_b \in \left\{\dfrac{3\pi}{4},\dfrac{\pi}{4}\right\}$, $\delta = 0$

$$BT = \left| \cos\left(\frac{\pi}{2} - \frac{3\pi}{4}\right) + \cos\left(\pi - \frac{3\pi}{4}\right) + \cos\left(\frac{\pi}{2} - \frac{\pi}{4}\right) - \cos\left(\pi - \frac{\pi}{4}\right) \right| = 2\sqrt{2} > 2 \tag{5.C.9}$$

Again, the quantum expectation values possess non-local correlations violating the BT.

Finally, what if angle δ is some arbitrary angle, so that both Bell bases enter into the expectation calculation? Again, let

$$O_{ab} = O_a O_b = \begin{bmatrix} 0 & e^{i\phi_a} \\ e^{-i\phi_a} & 0 \end{bmatrix}_a \begin{bmatrix} 0 & e^{i\phi_a} \\ e^{-i\phi_a} & 0 \end{bmatrix} . \tag{5.C.10}$$

All cross class Bell form terms are zero in (5.C.11), leaving only the terms computed above. Those surviving terms are weighted by the sinusoidal factors. Then the expectation value for O_{ab} is,

$$E(\phi_a,\phi_b) = \left\langle d_{out} \middle| O_{ab} \middle| d_{out} \right\rangle = \cos^2(\delta)\cos(\phi_a - \phi_b) + \sin^2(\delta)\cos(\phi_a + \phi_b) . \tag{5.C.11}$$

With $\{\phi_a\ \phi_b\} \in \left\{ \left\{\left\{\dfrac{\pi}{2},\pi\right\}_a,\left\{\dfrac{3\pi}{4},\dfrac{\pi}{4}\right\}_b\right\}, \left\{\left\{\dfrac{\pi}{4},\dfrac{3\pi}{4}\right\}_a,\left\{-\dfrac{\pi}{2},0\right\}_b\right\} \right\}$, as before,

$$BT = \cos^2(2\delta)\left| \sum E\left\{\left\{\dfrac{\pi}{4},\dfrac{3\pi}{4}\right\}_a,\left\{-\dfrac{\pi}{2},0\right\}_b\right\} \right| + \sin^2(2\delta)\left| \sum E\left\{\left\{\dfrac{\pi}{2},\pi\right\}_a,\left\{\dfrac{3\pi}{4},\dfrac{\pi}{4}\right\}_b\right\} \right|$$

$$= 2\sqrt{2}\left(\cos^2(2\delta) + \sin^2(2\delta)\right) = 2\sqrt{2} \tag{5.C.12}$$

(5.C.12) is independent of angle δ. We emphasize that cross terms from the BS giving rise to two photon coincidences in either path have been discarded.

Appendix 5.D

The full system matrix is given in Table 11. It's the matrix on the left. On the right is its partial transpose. Their eigenvalues are the sets {15 zeroes, 1} and {12 zeroes, -1/2, 1/2, 1/2, 1/2} respectively.

Table 11 Full Density Matrix and its Partial Transpose

vb;vb	vb;vh	vb;hb	vb;ha	va;vb	va;va	va;hb	va;ha	hb;vb	hb,va	hb,hb	hb;ha	ha;vb	ha;va	ha;hb	ha;ha
0000	0001	0010	0011	0100	0101	0110	0111	1000	1001	1010	1011	1100	1101	1110	1111
0	1	2	3	4	5	6	7	8	9	10	11	12	13	14	15

$$
\begin{bmatrix}
\frac{s^2}{8} & \frac{s^2}{8} & \frac{cs}{8} & -\frac{cs}{8} & \frac{s^2}{8} & \frac{s^2}{8} & \frac{cs}{8} & -\frac{cs}{8} & \frac{cs}{8} & \frac{cs}{8} & \frac{c^2}{8} & \frac{c^2}{8} & -\frac{cs}{8} & -\frac{cs}{8} & \frac{c^2}{8} & \frac{c^2}{8} \\
\frac{s^2}{8} & \frac{s^2}{8} & \frac{cs}{8} & -\frac{cs}{8} & \frac{s^2}{8} & \frac{s^2}{8} & \frac{cs}{8} & -\frac{cs}{8} & \frac{cs}{8} & \frac{cs}{8} & \frac{c^2}{8} & \frac{c^2}{8} & -\frac{cs}{8} & -\frac{cs}{8} & \frac{c^2}{8} & \frac{c^2}{8} \\
\frac{cs}{8} & \frac{cs}{8} & \frac{c^2}{8} & \frac{c^2}{8} & \frac{cs}{8} & \frac{cs}{8} & \frac{c^2}{8} & \frac{c^2}{8} & \frac{s^2}{8} & \frac{s^2}{8} & \frac{cs}{8} & \frac{cs}{8} & \frac{s^2}{8} & \frac{s^2}{8} & \frac{cs}{8} & \frac{cs}{8} \\
-\frac{cs}{8} & -\frac{cs}{8} & \frac{c^2}{8} & \frac{c^2}{8} & -\frac{cs}{8} & -\frac{cs}{8} & \frac{c^2}{8} & \frac{c^2}{8} & \frac{s^2}{8} & \frac{s^2}{8} & \frac{cs}{8} & \frac{cs}{8} & \frac{s^2}{8} & \frac{s^2}{8} & \frac{cs}{8} & \frac{cs}{8} \\
\frac{s^2}{8} & \frac{s^2}{8} & \frac{cs}{8} & -\frac{cs}{8} & \frac{s^2}{8} & \frac{s^2}{8} & \frac{cs}{8} & -\frac{cs}{8} & \frac{cs}{8} & \frac{cs}{8} & \frac{c^2}{8} & \frac{c^2}{8} & -\frac{cs}{8} & -\frac{cs}{8} & \frac{c^2}{8} & \frac{c^2}{8} \\
\frac{s^2}{8} & \frac{s^2}{8} & \frac{cs}{8} & -\frac{cs}{8} & \frac{s^2}{8} & \frac{s^2}{8} & \frac{cs}{8} & -\frac{cs}{8} & \frac{cs}{8} & \frac{cs}{8} & \frac{c^2}{8} & \frac{c^2}{8} & -\frac{cs}{8} & -\frac{cs}{8} & \frac{c^2}{8} & \frac{c^2}{8} \\
\frac{cs}{8} & \frac{cs}{8} & \frac{c^2}{8} & \frac{c^2}{8} & \frac{cs}{8} & \frac{cs}{8} & \frac{c^2}{8} & \frac{c^2}{8} & \frac{s^2}{8} & \frac{s^2}{8} & \frac{cs}{8} & \frac{cs}{8} & \frac{s^2}{8} & \frac{s^2}{8} & \frac{cs}{8} & \frac{cs}{8} \\
-\frac{cs}{8} & -\frac{cs}{8} & \frac{c^2}{8} & \frac{c^2}{8} & -\frac{cs}{8} & -\frac{cs}{8} & \frac{c^2}{8} & \frac{c^2}{8} & \frac{s^2}{8} & \frac{s^2}{8} & \frac{cs}{8} & \frac{cs}{8} & \frac{s^2}{8} & \frac{s^2}{8} & \frac{cs}{8} & \frac{cs}{8} \\
\frac{cs}{8} & \frac{cs}{8} & \frac{s^2}{8} & \frac{s^2}{8} & \frac{cs}{8} & \frac{cs}{8} & \frac{s^2}{8} & \frac{s^2}{8} & \frac{c^2}{8} & \frac{c^2}{8} & \frac{cs}{8} & \frac{cs}{8} & \frac{c^2}{8} & \frac{c^2}{8} & \frac{cs}{8} & \frac{cs}{8} \\
\frac{cs}{8} & \frac{cs}{8} & \frac{s^2}{8} & \frac{s^2}{8} & \frac{cs}{8} & \frac{cs}{8} & \frac{s^2}{8} & \frac{s^2}{8} & \frac{c^2}{8} & \frac{c^2}{8} & \frac{cs}{8} & \frac{cs}{8} & \frac{c^2}{8} & \frac{c^2}{8} & \frac{cs}{8} & \frac{cs}{8} \\
\frac{c^2}{8} & \frac{c^2}{8} & \frac{cs}{8} & \frac{cs}{8} & \frac{c^2}{8} & \frac{c^2}{8} & \frac{cs}{8} & \frac{cs}{8} & \frac{cs}{8} & \frac{cs}{8} & \frac{s^2}{8} & \frac{s^2}{8} & \frac{cs}{8} & \frac{cs}{8} & \frac{s^2}{8} & \frac{s^2}{8} \\
\frac{c^2}{8} & \frac{c^2}{8} & \frac{cs}{8} & \frac{cs}{8} & \frac{c^2}{8} & \frac{c^2}{8} & \frac{cs}{8} & \frac{cs}{8} & \frac{cs}{8} & \frac{cs}{8} & \frac{s^2}{8} & \frac{s^2}{8} & \frac{cs}{8} & \frac{cs}{8} & \frac{s^2}{8} & \frac{s^2}{8} \\
-\frac{cs}{8} & -\frac{cs}{8} & \frac{s^2}{8} & \frac{s^2}{8} & -\frac{cs}{8} & -\frac{cs}{8} & \frac{s^2}{8} & \frac{s^2}{8} & \frac{c^2}{8} & \frac{c^2}{8} & \frac{cs}{8} & \frac{cs}{8} & \frac{c^2}{8} & \frac{c^2}{8} & \frac{cs}{8} & \frac{cs}{8} \\
-\frac{cs}{8} & -\frac{cs}{8} & \frac{s^2}{8} & \frac{s^2}{8} & -\frac{cs}{8} & -\frac{cs}{8} & \frac{s^2}{8} & \frac{s^2}{8} & \frac{c^2}{8} & \frac{c^2}{8} & \frac{cs}{8} & \frac{cs}{8} & \frac{c^2}{8} & \frac{c^2}{8} & \frac{cs}{8} & \frac{cs}{8} \\
\frac{c^2}{8} & \frac{c^2}{8} & \frac{cs}{8} & \frac{cs}{8} & \frac{c^2}{8} & \frac{c^2}{8} & \frac{cs}{8} & \frac{cs}{8} & \frac{cs}{8} & \frac{cs}{8} & \frac{s^2}{8} & \frac{s^2}{8} & \frac{cs}{8} & \frac{cs}{8} & \frac{s^2}{8} & \frac{s^2}{8} \\
\frac{c^2}{8} & \frac{c^2}{8} & \frac{cs}{8} & \frac{cs}{8} & \frac{c^2}{8} & \frac{c^2}{8} & \frac{cs}{8} & \frac{cs}{8} & \frac{cs}{8} & \frac{cs}{8} & \frac{s^2}{8} & \frac{s^2}{8} & \frac{cs}{8} & \frac{cs}{8} & \frac{s^2}{8} & \frac{s^2}{8}
\end{bmatrix}
$$

Eigenvalues

$\{0,0,0,0,0,0,0,0,0,0,0,0,0,0,0, \mathbf{1}\}$ $\{\mathbf{-1/2}, 1/2, 1/2, 1/2, 0,0,0,0,0,0,0,0,0,0,0,0\}$

6 Summary

Title: Investigating Quantum Data Encrypted Modulation States

Reporting Period: FY14

Lab Task Manager: Dr. David H. Hughes

Phone: 315-330-4122/DSN 587-4122/ **Email:** david.hughes.16@us.af.mil

AFOSR Program Manager: Dr. Arje Nachman

Research Objectives: Investigate modulated optical signals, both quantum and classical, for information confidentiality, integrity, and availability

6.1 Technical Work

Simulation and measurement of the noise sources in coherent states of light is being conducted. Over and above the quantum noise of light, in which recent physical cryptographic systems utilize to impart randomness to a ciphertext, additional noise sources can have an even more debilitating effect on attempts to decrypt ciphertext. These latter sources of noise include detection system thermal noise as well as source laser phase drift noise.

A basic comparative study between long wavelength infrared (LWIR) verses short wavelength infrared (SWIR) propagation in fair and inclement weather is being conducted. Currently the communication bands under study are 1.5 and 10 micron bands. Despite the huge infrastructure devoted to the 1.5 micron band, work in the 10 micron band by several workers, including AFRL/RITE engineers, indicates that propagation in the 10 micron band is more robust in free space optics. That translates to greater information availability.

A combined optical/RF network is under development between Stockbridge and Rome. Currently, the optical band is primarily 1.5 micron band carrier frequencies; turbulence mitigation is accomplished by curvature adaptive optics. Planned is deployment of the LWIR/SWIR comparison experiment system over the longer range provided by the Rome/Stockbridge link as well as a coherent state quantum data encryption system.

We asked the question: Is polarization entanglement preserved in transit through the device? If not, can the device be modified to preserve the entanglement? Through modeling we found indications that polarization entanglement can be preserved and used in quantum key distribution.

Table 12 Resource Dispersal FY14

Government Salaries (6.1) Basic	$107,000
Onsite Contractor Support (6.1 Basic)	$99,640
Equipment (6.1 Basic)	$73,360